

Monitoring Quantum Simulators via Quantum Non-Demolition Couplings to Atomic Clock Qubits

Denis V. Vasilyev,^{1,2,*} Andrey Grankin,^{1,2,*} Mikhail A. Baranov,^{1,2} Lukas M. Sieberer,^{1,2} and Peter Zoller^{1,2}

¹*Center for Quantum Physics, University of Innsbruck, 6020 Innsbruck, Austria*

²*Institute for Quantum Optics and Quantum Information of the Austrian Academy of Sciences, 6020 Innsbruck, Austria*

(Dated: May 4, 2022)

We discuss monitoring the time evolution of an analog quantum simulator via a quantum non-demolition (QND) coupling to an auxiliary ‘clock’ qubit. The QND variable of interest is the ‘energy’ of the quantum many-body system, represented by the Hamiltonian of the quantum simulator. We describe a physical implementation of the underlying QND Hamiltonian for Rydberg atoms trapped in tweezer arrays using laser dressing schemes for a broad class of spin models. As an application, we discuss a quantum protocol for measuring the spectral form factor of quantum many-body systems, where the aim is to identify signatures of ergodic vs. non-ergodic dynamics, which we illustrate for disordered 1D Heisenberg and Floquet spin models on Rydberg platforms. Our results also provide the physical ingredients for running quantum phase estimation protocols for measurement of energies, and preparation of energy eigenstates for a specified spectral resolution on an analog quantum simulator.

I. INTRODUCTION

In the standard scenario of analog quantum simulation, a broad and tunable class of many-body Hamiltonians of interest is designed based on the resources provided by a particular physical platform. Examples in different physical platforms include spin models realized with Rydberg tweezer arrays [1–7] (for review see [8]), trapped ions [9–11] or superconducting qubits [12, 13], or Hubbard models realized with bosonic and fermionic atoms in optical lattices [14–16]. The physical realization of these Hamiltonians then allows the study of equilibrium and non-equilibrium phenomena, where the quantities of interest characterizing the quantum many-body state are spin- or site-occupation correlation functions. These are inferred from (destructive) site-resolved readout of spins, or in the case of Hubbard models from quantum gas microscopy.

In contrast, we will be interested below in a setting where we learn the state and dynamics of the many-body system by entangling the state of the quantum simulator with an auxiliary quantum system, followed by measurement of the auxiliary degrees of freedom, as illustrated in Fig. 1(a). In its simplest form, this auxiliary quantum system is a single qubit acting as a ‘clock’ [17, 18] (or ‘control’) qubit, which can be manipulated by single qubit operations (rotations). However, the following considerations generalize immediately also to a multi-qubit setting, where the auxiliary system represents a small scale quantum memory or quantum computer.

At the heart of our considerations is the quantum non-demolition (QND) Hamiltonian

$$\mathcal{H}_{\text{QND}} = H_{\text{spin}} \otimes |0\rangle_c \langle 0| \quad (1)$$

which generates the QND gate

$$\mathcal{U}_{\text{QND}}(t) = \exp[-i\mathcal{H}_{\text{QND}}t],$$

entangling the quantum simulator with a clock qubit. To be specific, we assume a spin model with Hamiltonian H_{spin} for the simulator, and we denote by $\{|0\rangle_c, |1\rangle_c\}$ the logical states of the clock qubit [19]. The above Hamiltonian is QND, with H_{spin} the ‘energy’ of the quantum many-body system, which plays the role of the QND variable. To illustrate the action of the above QND gate $\mathcal{U}_{\text{QND}}(t)$, consider a quantum simulator prepared in superposition $|\psi_{\text{spin}}\rangle = \sum_{\ell} c_{\ell} |\ell\rangle$ of energy eigenstates, $H_{\text{spin}}|\ell\rangle = E_{\ell}|\ell\rangle$ with eigenenergies E_{ℓ} . Under the QND gate, an initial state $|\Psi(t=0)\rangle = |\psi_{\text{spin}}\rangle \otimes |+\rangle_c$ of the joint quantum simulator prepared in $|\psi_{\text{spin}}\rangle$ and the control qubit prepared in the superposition state $|+\rangle_c = \frac{1}{\sqrt{2}}(|0\rangle_c + |1\rangle_c)$ will evolve according to

$$\begin{aligned} |\Psi(t=0)\rangle &\rightarrow |\Psi(t)\rangle = \mathcal{U}_{\text{QND}}(t) |\Psi(0)\rangle \\ &= \sum_{\ell} c_{\ell} |\ell\rangle \otimes \frac{1}{\sqrt{2}} (e^{-iE_{\ell}t} |0\rangle_c + |1\rangle_c). \end{aligned}$$

Thus the superposition of many-body energy eigenstates gets entangled with the phase of the Bloch vector of the clock qubit rotating in the xy -plane on the Bloch sphere. A readout of this phase via the clock qubit provides us with a QND measurement of ‘the energy’ of the quantum many-body system. In a broader context, we note that this QND gate is also the basic building block of quantum algorithms like quantum phase estimation (QPE) [20–22] to measure energies of the many-body spin system, and prepare corresponding eigenstates with a prescribed spectral resolution. We will use such features below in a protocol to measure the spectral form factor (SFF), where we access correlations between eigenenergies E_{ℓ} , encoded through a Fourier transform, via the clock qubit.

In the present paper we will first address the challenge of implementing the QND Hamiltonian (1) and QND gate

* Equal contribution

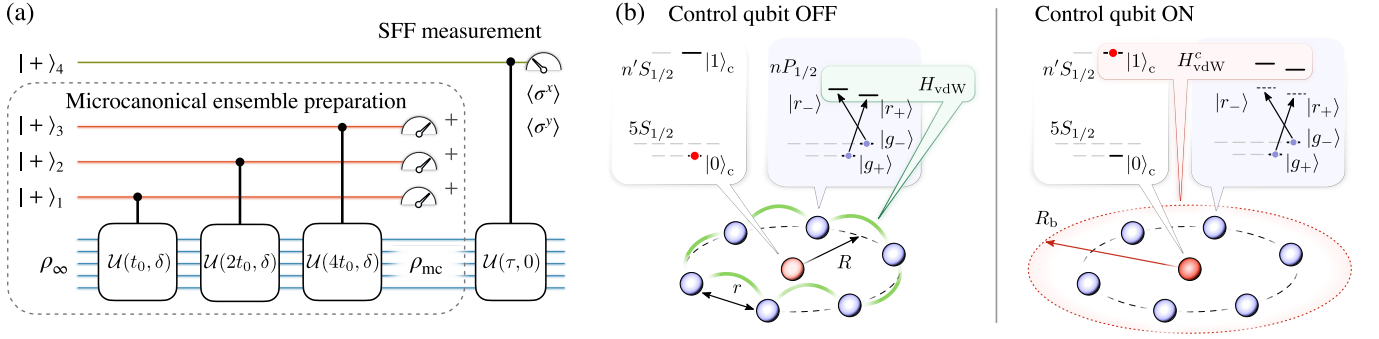


FIG. 1. (a) Quantum circuit employing a QND coupling of the quantum simulator to clock qubits to measure SFF. (Dashed block) The simulator spins (blue) initialized in the infinite temperature ensemble ρ_∞ are entangled with $M = 3$ control qubits (red) prepared in states $|+\rangle_c = (|0\rangle_c + |1\rangle_c)/\sqrt{2}$ via the QND gate $\mathcal{U}(t_m, \delta) = \exp\{-i[(H_{\text{spin}} - \delta) \otimes |0\rangle_c \langle 0|] t_m\}$. Postselecting measurement results of the control qubits allows one to project the spins into a microcanonical state ρ_{mc} . The simulator in the state ρ_{mc} is once again entangled with the clock qubit (green) to measure the SFF (see Sec. III). Alternatively, the protocol can be realized with a single clock qubit via sequential entanglement and measurement cycles. (b) Engineering the QND Hamiltonian (1) with Rydberg-dressed atoms. (Left panel) The control qubit (red) in the state $|0\rangle_c$ does not affect the evolution of the simulator spins (blue) arranged in a ring of radius R around the control atom. The spins (separated by a distance r) are represented by the hyperfine ground states $|g_\pm\rangle$ of ^{87}Rb and interact via virtually excited Rydberg states $|r_\pm\rangle$. (Right panel) The control qubit excited to the Rydberg state $|1\rangle_c$ breaks the dressing scheme for the simulator atoms within the Rydberg blockade radius R_b , thus, blocking the free evolution and realizing the controlled unitary $\mathcal{U}_{\text{QND}}(t)$.

for a broad class of freely designable spin models in a quantum simulator in atomic physics setups. Remarkably, as we show in Sec. II, this can be achieved with Rydberg tweezer platforms [1–7] using laser dressing schemes [23–28], and by employing a Rydberg blockade mechanism between the clock qubit and the simulator atoms to implement the QND Hamiltonian (1). Second, we wish to explore and illustrate the application of quantum protocols, which build on the above QND gate, providing access to novel quantum many-body observables of interest under experimentally realistic conditions. A relevant example is provided by measurement of the spectral form factor (SFF), as discussed in context of [29–32], where the aim is to identify signatures of ergodic vs. non-ergodic dynamics without an explicit spectroscopic study [33–35] of the energy spectrum. In Sec. III we describe a protocol, where the SFF can be measured via QND couplings to a clock qubit. We illustrate this protocol and its performance with simulated measurement runs for the disordered 1D Heisenberg model and Floquet models, which can be implemented with our techniques on Rydberg platforms.

The paper is organized as follows. In Sec. II we discuss implementation of the QND Hamiltonian with Rydberg tweezer arrays. The properties of the SFF in Hamiltonian systems are briefly summarized in Sec. III, where we also present the protocol for preparation of the initial state (Sec. III B 1) and the protocol for the SFF measurement together with the discussion of its experimental limitations (Sec. III B 2). The SFF of Floquet systems and the corresponding measurement protocol are considered in Sec. IV, and we conclude in Sec. V.

II. PHYSICAL REALIZATION OF \mathcal{H}_{QND} IN RYDBERG TWEEZER ARRAYS

The challenge is to implement \mathcal{H}_{QND} , Eq. (1), for a broad and tunable class of spin models H_{spin} on a given physical platform. The relevant example below is the disordered 1D Heisenberg spin-1/2 model,

$$H_{\text{spin}} = \sum_{i < j=1}^L \sum_{\eta=x,y,z} J_{ij}^{(\eta)} \sigma_i^\eta \sigma_j^\eta + \sum_{i=1}^L h_i^z \sigma_i^z, \quad (2)$$

or, to be more specific

$$H_{\text{spin}} = J \sum_{i=1}^L \left\{ (\sigma_i^x \sigma_{i+1}^x + \sigma_i^y \sigma_{i+1}^y + \Delta \sigma_i^z \sigma_{i+1}^z) + J_2 (\sigma_i^x \sigma_{i+2}^x + \sigma_i^y \sigma_{i+2}^y) + \Delta_2 \sigma_i^z \sigma_{i+2}^z \right\} + \sum_{i=1}^L h_i^z \sigma_i^z. \quad (3)$$

with designable *single* particle and *two-body* (interaction) terms. In implementing \mathcal{H}_{QND} we are required to implement the *two* and *three-body* terms involving the control qubit as $\mathcal{H}_{\text{QND}} = H_{\text{spin}} \otimes |0\rangle_c \langle 0|$.

Rydberg tweezer arrays in 1D, 2D and 3D [1–7] provide the tools to design a broad class of spin Hamiltonians H_{spin} via Rydberg dressing [23–28]. Here long-lived atomic (hyperfine) ground states are trapped in the optical tweezer, and play the role of the spins in our quantum simulator, while the two-body interactions are engineered by admixing weakly to the ground state via off-resonant

laser dressing the (strong) van der Waals interactions between Rydberg states [36, 37]. Remarkably, the *same* ‘dressing toolbox’ which allow to design H_{spin} also provide us with a recipe to engineer \mathcal{H}_{QND} .

As originally discussed in [38], see also [39–42], interactions engineered via laser dressing can be turned on and off by preparing a control spin (or qubit) which is in the ground state $|0\rangle_c$ or a Rydberg state $|1\rangle_c$, respectively [see Fig. 1(b) left and right panel, respectively]. If the control spin is in the ground state, the control spin does not interact with the system spins, and thus the Hamiltonian H_{spin} is realized, as discussed above. On the other hand, for the control spin in the Rydberg state $|1\rangle_c$, the long-range character and strength of Rydberg-Rydberg interactions will, via the *dipole blockade mechanism*, detune the Rydberg states of the simulator atoms, thus effectively turning off the dressing interactions, i.e. we have $\mathcal{H}_{\text{QND}} = H_{\text{spin}} \otimes |0\rangle_c \langle 0|$. We will analyze this below in a realistic atomic physics setting.

A. Hamiltonian for the simulator and control qubit

We consider the setup outlined in Fig. 1(b). L atoms trapped in optical tweezers are arranged in a ring repre-

senting a 1D quantum simulator of spin-1/2 with periodic boundary conditions. The distance r between simulator atoms is assumed to be larger than $2.4 \mu\text{m}$ as discussed in Appendix (A 3). The control qubit is represented by an atom trapped in the center of the ring. In Fig. 1(b) we show the atomic level structure for the atoms representing the quantum simulator, and the control atom. The spin-1/2 degrees of freedom of the simulator are encoded in two long-lived hyperfine ground states $|g_{\pm}\rangle$ with energies $E_{g_{\pm}}$. These are coupled to Rydberg states $|g_{\pm}\rangle \rightarrow |r_{\pm}\rangle$ with energies $E_{r_{\pm}}$ by two off-resonant lasers with respective frequencies ω_{\pm} and detunings $\Delta_{\pm} = \omega_{\pm} - E_{r_{\pm}} + E_{g_{\pm}} \gg \Omega_{\pm}$, and Ω_{\pm} corresponding Rabi frequencies. The ground state of the control qubit is $|0\rangle_c$ with energy E_{gc} , while $|1\rangle_c$ is a Rydberg state with energy E_{rc} . We drive the control atom transition with a laser of frequency ω_c which is tuned near resonance with detuning $\Delta_c = \omega_c - E_{rc} + E_{gc}$. The corresponding Rabi frequency is Ω_c . In our protocol, the control qubit is prepared initially in a superposition state of ground and excited state with a $\pi/2$ -pulse.

The Hamiltonian of the total system is $H_{\text{tot}} = H_s + H_c + H_{sc}$, written as sum of the simulator and control atom Hamiltonians, and the simulator-control interaction. These are given by

$$H_s = \left\{ \sum_{i=1}^L \sum_{\alpha=\pm} [E_{g_{\alpha}} |g_{\alpha}\rangle_i \langle g_{\alpha}| + E_{r_{\alpha}} |r_{\alpha}\rangle_i \langle r_{\alpha}| + (\Omega_{\alpha} |g_{\alpha}\rangle_i \langle r_{\alpha}| e^{-i\omega_{\alpha}t} + \text{H.c.})] + \sum_{i<j}^L H_{\text{vdW}}^{(i,j)} \right\} \otimes \mathbb{I}_c, \quad (4)$$

$$H_c = \mathbb{I}_s \otimes [E_{gc} |0\rangle_c \langle 0| + E_{rc} |1\rangle_c \langle 1| + (\Omega_c |0\rangle_c \langle 1| e^{-i\omega_c t} + \text{H.c.})], \quad (5)$$

$$H_{sc} = \sum_{i=1}^L H_{\text{vdW}}^{(i,c)}. \quad (6)$$

Here $H_{\text{vdW}}^{(i,j)}$ is the van der Waals interaction between the Rydberg manifolds $\{|r_{\pm}\rangle_i\}$ and $\{|r_{\pm}\rangle_j\}$ of simulator atoms i and j , and $H_{\text{vdW}}^{(i,c)}$ denotes the van der Waals interaction between the control atom in $|1\rangle_c$ and Rydberg atom $\{|r_{\pm}\rangle_i\}$.

As stated above, in our model, the effective spin-1/2 of the quantum simulator is encoded in ground states $|g_{\pm}\rangle$ of the simulator atoms (see, for example, [36] and [43] for a specific choice). Following [36], an effective spin-spin interaction is obtained by admixing to these ground states with a laser a fine-structure split Rydberg state. We note that it is the combination of a *fine-structure* resolved Rydberg manifold (i.e. the spin-orbit coupling) together with the van der Waals interaction (away from Förster resonances [44]) which provides the physical mechanism for the effective spin-spin interactions in the ground state manifold, and determines the spin models which can be realized in this setup (see Appendices A and B). To be specific, we assume below

^{87}Rb with Rydberg states $|r_{\pm}\rangle = |nP_{1/2}, m_j = \pm 1/2\rangle$ for the simulator atoms, and Rydberg state of the control atom $|n'S_{1/2}, m_j = 1/2\rangle$. In the basis $\{|r_{\pm}\rangle_i \otimes |r_{\pm}\rangle_j\}$ of the given Rydberg manifold, the interaction $H_{\text{vdW}}^{(i,j)}$ is then represented by a 4×4 matrix [43],

$$H_{\text{vdW}}^{(i,j)} = \frac{1}{r_{ij}^6} \left[C_6 \mathbb{I}_4 - \tilde{C}_6 \mathbb{D}_0(\theta_{ij}, \phi_{ij}) \right]. \quad (7)$$

Here C_6 and \tilde{C}_6 are van der Waals interaction constants, \mathbb{I}_4 is the identity matrix, and \mathbb{D}_0 a 4×4 matrix with θ_{ij}, ϕ_{ij} angles representing the axis connecting the pair of atoms i, j with distance r_{ij} . Explicit expressions for these quantities are provided in Appendix A 1. In a similar way, the van der Waals interaction between the simulator atom i and control atom c has the form

$$H_{\text{vdW}}^{(i,c)} \approx \frac{C'_6}{r_{ic}^6} \sum_{\alpha=\pm} |r_{\alpha}\rangle_i \langle r_{\alpha}| \otimes |1\rangle_c \langle 1|, \quad (8)$$

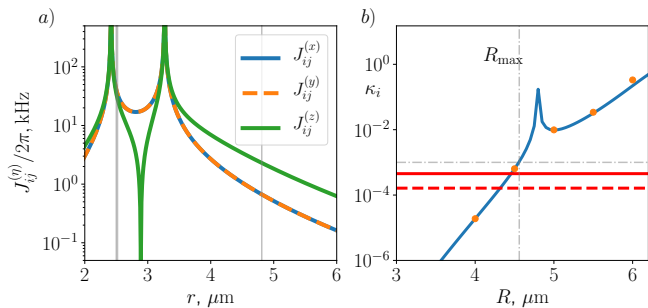


FIG. 2. Engineered QND Hamiltonian. (a) Spin-spin interaction constants as a function of interatomic distance r . Gray vertical lines indicate the nearest and next-nearest neighbor positions. (b) Decoherence parameters κ_1 (red solid), κ_2 (red dashed) and κ_3 (analytic blue solid and numeric orange dots) for $L \sim 10$ spins. Parameters of the dressing are: $\xi_{\pm} \equiv \Omega_{\pm}/\Delta_{\pm} = 0.2$, $\Delta_{\pm} = -9$ MHz. Principle quantum number of Rydberg atoms are $n = 60$, $n' = 71$.

with C'_6 the corresponding van der Waals coefficient. Here we made the assumption that C'_6 is independent of the state $|r_{\pm}\rangle$ (see Appendix A 2). Thus, conditional to the control atom to be in the Rydberg state $|1\rangle_c$, the Rydberg energies of the simulator atoms are shifted by $E_{r\pm} \rightarrow E_{r\pm} + C'_6/r_{ic}^6$, which for the ring geometry of Fig. 1(b) provides an identical shift for all simulator atoms. In the spirit of the Rydberg blockade mechanism we assume this shift to be large. Thus, for a control atom in the ground state $|0\rangle_c$ the dressing lasers ω_{\pm} are detuned from the Rydberg states $|r_{\pm}\rangle_i$ by Δ_{\pm} , while the presence of a control atom in $|1\rangle_c$ will detune these excited states by $\Delta_{\pm} - C'_6/r_{ic}^6$. For a control atom in $|0\rangle_c$ the dressing lasers will thus induce interactions between the effective ground state spin-1/2 by admixing the Rydberg-Rydberg interactions $H_{\text{vdW}}^{(i,j)}$ to the ground state manifold, while a control atom in $|1\rangle_c$ detunes the Rydberg states, and thus effectively shuts off Rydberg dressing.

B. QND Hamiltonian and imperfections

The derivation of \mathcal{H}_{QND} proceeds now by a perturbative elimination of the Rydberg manifold of the simulator atoms. First, for the control atom in the ground state $|0\rangle_c$, and $\Omega_c = 0$, the dressing lasers for the simulator atoms are described by the detunings Δ_{\pm} , as discussed above, and the relevant perturbation parameter for elimination of the Rydberg states is $\xi_{\pm} = \Omega_{\pm}/\Delta_{\pm} \ll 1$. This yields an effective dynamics as spin-1/2 model for the dressed ground states $|\tilde{g}_{\pm}\rangle_i$ with effective spin-1/2 Hamiltonian denoted by H_{spin} . The design of the desired spin Hamiltonians via dressing schemes by an appropriate choice of the atomic and laser configurations, and van der Waals interaction for a given geometry was discussed by [36]. In Appendix B we provide a derivation for the disordered 1D Heisenberg chain in the form (3). There we list explicit

expressions for the $J^{(x,y,z)}$, h etc. in Eqs. (B9-B12) of Appendix B as functions of the microscopic atomic parameters. Figure 2(a) shows the values of the spin-spin interaction constants $J_{ij}^{(\eta)}$ as a function of the interatomic distance for a particular dressing scheme parameters.

Second, we repeat this derivation for the control atom in the excited state $|1\rangle_c$ which amounts to replacing the detunings $\Delta_{\pm} \rightarrow \Delta_{\pm} - C'_6/r_{ic}^6$ in the expressions for the parameters of the Hamiltonian (B6) of Appendix B. This results in a spin Hamiltonian which we denote by H'_{spin} , with the same structure as H_{spin} , but strongly suppressed couplings $J' \ll J$ etc. After combining the two cases, we obtain the Hamiltonian describing the coupling between the simulator and the control qubit

$$\tilde{\mathcal{H}} = H_{\text{spin}} \otimes |0\rangle_c \langle 0| + H'_{\text{spin}} \otimes |1\rangle_c \langle 1|.$$

If H_{spin} and H'_{spin} commute, $\tilde{\mathcal{H}}$ is equivalent to the QND Hamiltonian (1) with $H_{\text{spin}} \rightarrow H_{\text{spin}} - H'_{\text{spin}}$. In the opposite case, H'_{spin} results in errors in the entangling gate $\mathcal{U}_{\text{QND}}(t)$, with the error rate characterized by a dimensionless parameter $\kappa_3 = |H'_{\text{spin}}|/|H_{\text{spin}}|$, where $|\dots|$ denotes the difference between the maximal and the minimal eigenvalues of the corresponding operator. Another source of error is related to spontaneous emission of Rydberg states of the control and simulator atoms, with error rates characterized by $\kappa_1 \equiv \gamma'_d/|H_{\text{spin}}|$ and $\kappa_2 \equiv \xi_{\pm}^2 \gamma_d L/|H_{\text{spin}}|$, respectively, where γ'_d and γ_d are the corresponding spontaneous emission rates [see Fig. 2(b) and Appendix D for more details]. The maximal of κ_i determines the coherence time $t_{\text{coh}} \sim [|H_{\text{spin}}| \max\{\kappa_i\}]^{-1}$ below which the errors in the gate operation due to spontaneous emission and H'_{spin} can be ignored.

Thus for $t < t_{\text{coh}}$ the quantum simulator coupled to the control qubit can be described by the QND Hamiltonian Eq. (1)

$$\tilde{\mathcal{H}}_{\text{QND}} = (H_{\text{spin}} - \delta) \otimes |0\rangle_c \langle 0|, \quad (9)$$

which is written here in the rotating frame with respect to the laser of the control qubit, and we have set $\Omega_c = 0$ in H_c ($\Omega_c \neq 0$ is needed only during the preparation stage of the control qubit and for the measurement readout). In the above equation δ refers to a renormalized detuning of the control laser (see Appendix B).

III. MEASUREMENT OF THE SFF IN HAMILTONIAN SYSTEMS

For a generic quantum many-body system, the energy level statistics is an indicator which allows to distinguish between quantum ergodic and non-ergodic regimes [45–48]. Quantum ergodic (or chaotic) systems are characterized by eigenenergies statistics given by the Wigner-Dyson distribution [49] in a universality class of random matrices, and the eigenfunctions are delocalized over the configuration space. In contrast, non-ergodic quantum systems,

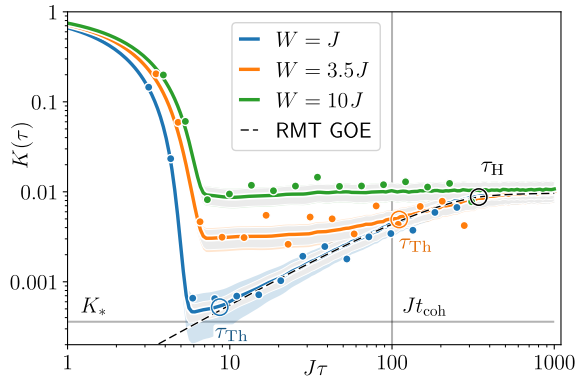


FIG. 3. Measurement of the spectral form factor $K(\tau)$ in the Heisenberg chain (3) of $L = 12$ spins for different disorder strengths W . The black dashed line represents the RMT prediction $K_{\text{GOE}}(\tau)$ (12). The color dots show the results of the simulated measurements of $K(\tau)$. The color solid lines and the shaded areas indicate, respectively, the numerical prediction for $K(\tau)$ and the root-mean-square error due to the shot noise and disorder averaging for the simulated $\simeq 2 \times 10^5$ experimental runs per data point. The gray areas show the contribution of averaging over 20 disorder realizations.

such as integrable models, display Poisson statistics of energy levels and localized wave-functions. These considerations apply not only to systems with time-independent Hamiltonians and their energy spectrum, but also to time-periodic Floquet systems [45] characterized by quasienergies.

An equivalent characterization of ergodic vs. non-ergodic dynamics is provided by the spectral form factor (SFF), where spectral features are displayed in the time domain, i.e. essentially as the Fourier transform of the two-point correlation function of the spectral density. For a many-body Hamiltonian H_{spin} with eigenenergies E_ℓ the SFF is defined as

$$K(\tau) = \overline{\left| \sum_{\ell} f(E_{\ell}) e^{-iE_{\ell}\tau} \right|^2} \quad (10)$$

$$\equiv \overline{\left| \text{tr}(e^{-iH_{\text{spin}}\tau} \rho_{\text{mc}}) \right|^2} \quad (11)$$

Here $f(E)$ is a nonnegative normalized smooth filter function of width ΔE covering a band in the middle of the energy spectrum, where the density of states is flat, thus probing the properties of typical states of the many-body system, while eliminating contributions from spectral edges. The overline indicates a possible disorder average. The second line of (10) rewrites the SFF in terms of the microcanonical density operator $\rho_{\text{mc}} = \sum_{\ell} f(E_{\ell}) |\ell\rangle \langle \ell|$ representing an initial density matrix. The SFF has been central in high-energy physics [29] and the recent discussion of the transition from many-body localization (MBL) to quantum chaos in a class of generic spin chains with disorder [30–32].

A. Properties of the SFF

To illustrate the generic behavior of SFF, we show in Fig. 3 a numerically calculated SFF for the disordered Heisenberg XXZ spin-1/2 chain of length $L = 12$ with Hamiltonian (3). A random local transverse field [last term in Eq. (3)] plays the role of disorder, with values $h_i \in [-W, W]$ drawn from a uniform distribution and W characterizing the disorder strength. We assume periodic boundary conditions, and consider the sector with zero total spin projection on the z -axis, $S_z = \sum_{i=1}^L \sigma_i^z = 0$. The choice of this model is based on the following considerations. First, it exhibits a transition from quantum chaos for weak disorder to many-body localization for strong disorder, and second, it belongs to the class of models, where the QND-gate and thus the SFF protocol of the following section can be implemented with the dressing scheme in Rydberg tweezer arrays (see Sec. II).

According to Fig. 3, for small times τ the SFF $K(\tau)$ decays from its initial value $K(0) = 1$ due to dephasing on a time scale $\sim 1/\Delta E$. Here $\Delta E \approx (E_{\text{max}} - E_{\text{min}})/6$, i.e., 1/6 of the width of the energy spectrum. The signature of quantum chaos is the existence of a ramp at long times τ : Random Matrix Theory (RMT) for the Gaussian orthogonal ensemble (GOE), which is applicable to systems obeying time-reversal symmetry, predicts

$$K_{\text{GOE}}(\tau) = K_{\infty} \begin{cases} 2\frac{\tau}{\tau_{\text{H}}} - \frac{\tau}{\tau_{\text{H}}} \log(1 + 2\frac{\tau}{\tau_{\text{H}}}), & 0 < \tau \leq \tau_{\text{H}}, \\ 2 - \frac{\tau}{\tau_{\text{H}}} \log\left(\frac{2\tau + \tau_{\text{H}}}{2\tau - \tau_{\text{H}}}\right), & \tau > \tau_{\text{H}}, \end{cases} \quad (12)$$

which is shown as dashed line in Fig. 3. In the formula above, $\tau_{\text{H}} = 2\pi/\delta_E \sim 2^L/L$ denotes the Heisenberg time associated with the mean level spacing $\delta_E = \langle E_{\ell+1} - E_{\ell} \rangle$ in the middle of the spectrum. Furthermore, $K_{\infty} = \sum_{\ell} f^2(E_{\ell})$, where the value of K_{∞} is equivalently given by the inverse of the number $N_{\Delta E}$ of the eigenstates in the energy interval ΔE , $K_{\infty} \approx N_{\Delta E}^{-1}$. As shown in Fig. 3, the RMT prediction agrees well with simulations for a finite size chain in the limit of weak disorder (blue line) for times $\tau > \tau_{\text{Th}}$, with τ_{Th} the Thouless time defined as the onset of the ramp [31]. The flattening with increasing disorder strength (orange and green lines) is indicative of the crossover towards nonergodic (MBL) behavior.

The Hamiltonian (3) is time-reversal symmetric and thus its chaotic phase is described by the GOE. As discussed in Appendix C, this model can also be realized with complex J , so that the chaotic phase is described by a GUE. In systems with broken time-reversal symmetry, $K(\tau)$ follows the RMT prediction for the Gaussian unitary ensemble (GUE),

$$K_{\text{GUE}}(\tau) = K_{\infty} \begin{cases} \frac{\tau}{\tau_{\text{H}}}, & 0 < \tau \leq \tau_{\text{H}}, \\ 1, & \tau > \tau_{\text{H}}. \end{cases} \quad (13)$$

Our SFF protocol below exploits repeated QND measurements of the control qubit to both prepare the desired

initial energy distribution $f(E)$ in (10) [see Fig. 1(a)], as well as to read the SFF (10). Challenges faced in measuring the SFF, and addressed below, are decoherence times in quantum simulators, relative to times required to identify the ‘ramp’, and the number of measurements required to provide clear signatures of both the ergodic and non-ergodic regimes. Figure 3 plots simulated measurements for a finite measurement budget which compare favorably with the (exact) numerical results for the SFF (solid lines). The question to be addressed is whether, with given experimental resources, it is possible to see the main characteristics of the SFF.

B. Measurement Protocol via QND-Coupling to a Control Qubit

An experimental protocol to measure the SFF in the Hamiltonian case will require: (i) the ability to prepare an initial (microcanonical) ensemble of states $\rho_{\text{mc}} = \sum_{\ell} f(E_{\ell}) |\ell\rangle \langle \ell|$ with a filter function $f(E)$ of given width ΔE in the center of the spectrum; (ii) the ability to resolve for a given number of measurements, and thus signal-to-noise ratio the baseline $K_{\infty} \approx N_{\Delta E}^{-1}$ and the value of the SFF around the Thouless time; and finally (iii) the ability to observe for a given decoherence time (part of) the ramp $\tau_{\text{Th}} < \tau < \tau_{\text{H}}$ and possibly the long time behavior of $K(\tau)$.

1. Preparation (verification) of a microcanonical ensemble

The first step of the protocol requires preparation of the microcanonical (MC) ensemble $\rho_{\text{mc}} = \sum_{\ell} f(E_{\ell}) |\ell\rangle \langle \ell|$. This can be achieved with a low resolution phase estimation algorithm (PEA), providing a probabilistic preparation of an energy band via repeated measurement of the control qubit. The PEA is based on the QND Hamiltonian (1), and requires a minimal number of measurements M of the control qubit to achieve a given measurement precision ΔE [20–22].

Figure 4 illustrates the idea of the preparation protocol. First, the many-body spin system initialized in a state ρ_{in} and the control qubit prepared in the state $|+\rangle_c$ are entangled by the QND interaction \mathcal{H}_{QND} (1) during a time t_0 . As a result the control qubit is rotated proportionally to the values of eigenenergies E_{ℓ} of the spin Hamiltonian (3). The time t_0 is chosen to maximally spread the full spectrum E_{ℓ} of the Hamiltonian H_{spin} over the equator of the control qubit Bloch sphere. After that, the control qubit measurement in $|\pm\rangle_c$ basis shrinks the populated energy window of the spins state by a factor of ~ 2 . Repeating the cycle with increasing interaction times t_m and postselecting “+” outcomes results in the state ρ_{mc} with a narrow energy distribution.

Figure 1(a) shows the quantum circuit for the full preparation procedure involving $M = 3$ control qubits entangled

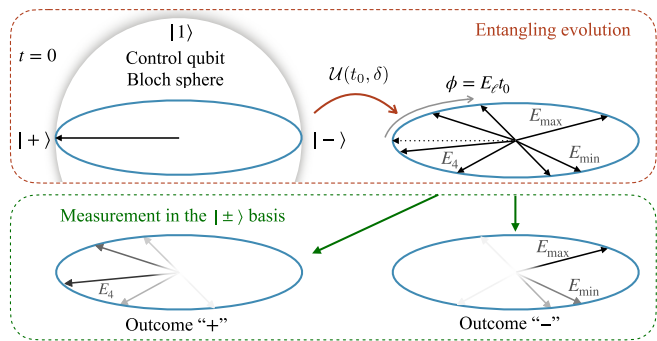


FIG. 4. The microcanonical ensemble preparation process. The first filtering step with interaction time t_0 is shown. The QND interaction (1) rotates the control qubit proportionally to the eigenenergy E_{ℓ} of the spin Hamiltonian (3). The measurement in the basis $|\pm\rangle$ leads to narrowing of the populated energy window of the spins state ρ_{out} . The shades of gray of the arrows corresponding to different E_{ℓ} represent the conditional probability for the eigenstate $|\ell\rangle$ to appear in ρ_{out} .

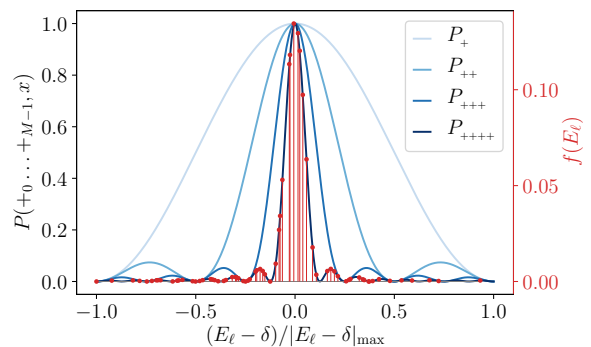


FIG. 5. The filter functions for $M = 1, 2, 3, 4$ filtering steps (control qubits) are shown in blue. The eigenstates probabilities $f(E_{\ell})$ filtered with $M = 4$ steps are shown in red.

with the simulator via

$$\mathcal{U}(t_m, \delta) = \exp \{-i[(H_{\text{spin}} - \delta) \otimes |0\rangle_c \langle 0|] t_m\}.$$

Note, that the same result can be achieved by performing sequential entanglement and measurement cycles with a single control qubit. The interaction times are chosen as $t_m \equiv 2^m t_0$, $m = 0, \dots, M-1$ where $t_0 \leq \pi/(|E_{\ell} - \delta|_{\text{max}})$. The renormalized detuning of the control laser δ introduced in Eq. (9) allows to tune the energy band of the state to be prepared. If we now select a run with all readouts “+ $_m$ ”, $m = 0, \dots, M-1$, then the initial state of the spin system is projected into the state ρ_{out} with a narrow distribution in the energy eigenbasis $|\ell\rangle$ (see Appendix E)

$$\langle \ell | \rho_{\text{out}} | \ell \rangle \propto p_{\ell} = P(+_0 \dots +_{M-1}, E_{\ell} - \delta) \langle \ell | \rho_{\text{in}} | \ell \rangle,$$

where

$$P(+_0 \dots +_{M-1}, x) = \left\{ \frac{\sin(2^M t_0 x)}{2^M \sin(t_0 x)} \right\}^2. \quad (14)$$

The success probability of the preparation is $p_{\text{mc}} \equiv \sum_{\ell} p_{\ell}$. The function (14) has a peak at $x = 0$ with a width $\sim 2^{-M}/t_0$, and, therefore, the conditional outcome state exhibits an exponential narrowing of the energy distribution/uncertainty around $E_{\ell} \approx \delta$. Note, however, that the variance of this distribution has the same scaling $\sim 2^{-M}/t_0^2$ due to the presence of long tails.

Following the above procedure, the microcanonical ensemble can be prepared by initializing the spin system in the infinite temperature state $\rho_{\text{in}} = \rho_{\infty} \propto \sum_{\ell} |\ell\rangle\langle\ell|$ and postselecting the outcome state with the probability $p_{\text{mc}} \sim 2^{-M}$. As a result, the spin system will be probabilistically prepared in the microcanonical ensemble $\rho_{\text{mc}} = \sum_{\ell} f(E_{\ell}) |\ell\rangle\langle\ell|$ with $f(E_{\ell}) \propto \sum_{\ell} P(+_0 \dots +_{M-1}, E_{\ell} - \delta)$. The state has the mean energy $\bar{E} = \text{Tr}\{H_{\text{spin}}\rho_{\text{mc}}\} = \delta$ and the bandwidth $\Delta E = \sqrt{\text{Tr}\{(H_{\text{spin}} - \delta)^2 \rho_{\text{mc}}\}} \sim 2^{-M/2}/t_0$. Note that the initial infinite temperature ensemble ρ_{∞} can be sampled by random initialization of individual spins in up and down states where we additionally apply the constraint $S_z = 0$ to probe the SFF in the zero-magnetization sector. An example of the resulting eigenstates probability distributions is shown in Fig. 5 for the Heisenberg chain (3) of $L = 8$ spins.

We remark that measuring the probability p_{mc} of the successful MC ensemble preparation allows one to estimate (see Appendix H for details) the Heisenberg time τ_{H} and the plateau value K_{∞} of the SFF as $\tau_{\text{H}} \simeq 2^{M+1}t_0\mathcal{D}p_{\text{mc}}$ and $K_{\infty} \simeq (2/3)(\mathcal{D}p_{\text{mc}})^{-1}$. Here \mathcal{D} is the Hilbert space dimension of the considered symmetry sector of the model. For the Heisenberg spin chain (3) with $S_z = 0$ we have $\mathcal{D} = C_L^{L/2} \approx \sqrt{2/\pi L}2^L$ with $C_L^{L/2}$ being the binomial coefficient (we assume L to be even). In the experiment the probability p_{mc} is given by the ratio of the number of successful preparation attempts to the total number of experimental runs. The estimated values of τ_{H} and K_{∞} uniquely determine the behavior of the SFF in the chaotic regime assuming RMT (dashed lines in Figs. 3 and 6).

The low resolution PEA procedure can also be used to verify that a given state consists of a superposition of energy eigenstates in a narrow energy interval ΔE around \bar{E} (MC ensemble): With $\delta = \bar{E}$, the appearance of $M \simeq 2 \log_2(|E_{\ell} - \delta|_{\text{max}}/\Delta E)$ successive “+” readouts with probability close to 1 signals that the given state has a desired energy variance. Further, if the state ρ_{in} contains a collection of excited states in a narrow energy interval created from some initial state by a time-dependent perturbation (see [33], for example), a MC state can be distilled with our procedure through several successive “+” readouts.

2. Protocol to measure the SFF

Following the preparation of the microcanonical ensemble ρ_{mc} , we perform the evolution for a time τ with the QND-Hamiltonian (1), and finally measure the expectation values of σ^x and σ^y for the control qubit, as shown

in the Fig. 5(a),

$$\begin{aligned} \langle \sigma^x(\tau) \rangle &= \text{Tr} \left\{ e^{-i\tau H_{\text{spin}} \otimes |0\rangle_c \langle 0|} \rho_{\text{mc}} \otimes |+\rangle_c \langle +| e^{i\tau H_{\text{spin}} \otimes |0\rangle_c \langle 0|} \sigma^x \right\} \\ &= \sum_{\ell} f(E_{\ell}) \cos(E_{\ell}\tau), \\ \langle \sigma^y(\tau) \rangle &= \sum_{\ell} f(E_{\ell}) \sin(E_{\ell}\tau), \end{aligned}$$

These provide us with $|\sum_{\ell} f(E_{\ell})e^{-iE_{\ell}\tau}|^2 \approx \langle \sigma^x(\tau) \rangle^2 + \langle \sigma^y(\tau) \rangle^2$ (see Appendix F). We obtain $K(\tau)$ by repeating this sequence for different disorder realizations and averaging the result.

The SFF measurement scheme realizes a QND measurement meaning that the initial state of the spin system is not heated up or destroyed after the interaction with the control qubit. It is, therefore, possible to reuse the once prepared ρ_{mc} for the measurement of $K(\tau)$ with different times τ_i (see Appendix G). The maximum number of recycling times N_{reuse} is restricted by the coherence time t_{coh} of the spin system as $\sum_{i=1}^{N_{\text{reuse}}} \tau_i \ll t_{\text{coh}}$.

3. Experimental challenges

An experimental realization of the SFF measurement faces two main challenges, which limit the achievable system sizes.

Time scales: – Propagation up to the Heisenberg time τ_{H} , which grows exponentially with the system size L , is limited by the finite coherence time of the quantum simulator. Thus, observation of the behavior of $K(\tau)$ at times $\tau \sim \tau_{\text{H}}$, requires coherence times $t_{\text{coh}} > \tau_{\text{H}} \sim 2^L/(JL)$. We note, however, that the effects of interest such as the transition to chaotic dynamics at the Thouless time τ_{TH} and the distinct behaviors of the SFF for quantum chaotic [$K(\tau) \sim \tau$] and integrable systems [$K(\tau) \sim \text{const.}$] take place at much shorter times to be compared with t_{coh} (see Appendix D).

Signal magnitude: – The second challenge is the exponentially small values of the SFF $\sim 2^{-L}$ at the characteristic times. The threshold signal level which can be distinguished from the shot noise after averaging over N_{d} realizations of disorder in the spin Hamiltonian and N measurements per one disorder realization is given by $K_* \equiv 2(1 + \sqrt{2})/(N\sqrt{N_{\text{d}}})$ (see Appendix F). Thus, the total number of experimental runs per data point necessary to resolve the features of interest in $K(\tau)$, is given by $N_{\text{run}} > 2^L\sqrt{N_{\text{d}}}/N_{\text{reuse}}$ for the probabilistic preparation of the initial MC ensemble (see Appendix D).

4. Numerical simulation of the SFF measurement

To demonstrate the feasibility of the SFF measurement with our protocol, we perform numerical simulations of the measurement process in the disordered Heisenberg

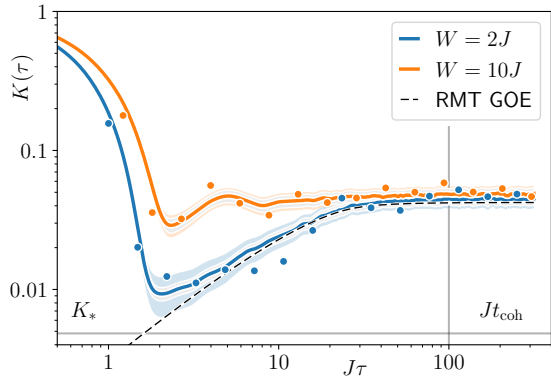


FIG. 6. Revealing the signatures of quantum chaos in the disordered Heisenberg chain of $L = 8$ spins. The colored dots show results of simulated measurements of $K(\tau)$ for two disorder strengths $W = 2J, 10J$. Solid lines show the corresponding theoretical $K(\tau)$ and the black dashed line represents the RMT prediction $K_{\text{GOE}}(\tau)$. The shaded areas show the root-mean-square error due to the shot noise and disorder averaging.

spin chain for various numbers L of spins. The simulation includes the probabilistic preparation of the initial state ρ_{mc} and averaging over finite numbers of disorder realizations and experimental runs.

The results are presented in Figs. 3 and 6. According to Fig. 6, a small system of $L = 8$ spins with the measurement budget of $N_{\text{run}} \simeq 10^4$ experimental runs per data point allows identification of the linear ramp in $K(\tau)$. This indicates the chaotic behavior with level repulsion in the Heisenberg model with a weak disorder $W = 2J$ (blue dots). In contrast, a strong disorder $W = 10J$ results in the localized behavior of the system dynamics (orange dots) lacking correlations in the distribution of the eigenenergies. The colored lines and the corresponding shaded areas represent the numerical prediction for $K(\tau)$ and the root-mean-square error of the simulated measurement, respectively. The black dashed line is the RMT prediction $K_{\text{GOE}}(\tau)$ Eq. (12).

The Thouless times τ_{Th} for various disorder strengths can be probed in a larger system of $L = 12$ spins as shown in Fig. 3. It is evident from the figure that the time τ at which the data points approach the RMT prediction $K_{\text{GOE}}(\tau)$ given by the black dashed line grows with the increase of the disorder strength W , which is compatible with the expected behavior of the Thouless time τ_{Th} . The root-mean-square error of the simulated measurement with $N_{\text{run}} \simeq 2 \times 10^5$ experimental runs per data point is shown with shaded areas around the solid lines indicating the numerical prediction for $K(\tau)$.

In both Figs. 3 and 6 the horizontal and vertical gray lines mark the shot noise threshold K_* and the coherence time $t_{\text{coh}} \sim 10^2 J^{-1}$ in our Rydberg setup (see Appendix D), respectively. For the system of $L = 8(12)$ spins we simulate MC ensemble preparation with $M = 3(5)$ filtering steps, perform averaging over $N_{\text{d}} = 100(20)$,

and include recycling of the prepared MC ensemble for $N_{\text{reuse}} = 10$ times. The parameters of the Heisenberg model (3) for both system sizes are $\Delta = 1$, $J_2 = 0.1$, $\Delta_2 = 0.3$.

It is important to stress, that in both cases of $L = 8$ and $L = 12$, the $K_{\text{GOE}}(\tau)$ curves (black dashed lines) are completely determined by the plateau value K_{∞} for $\tau \rightarrow \infty$ and by the Heisenberg time τ_{H} , both of which can be independently estimated as outlined in Sec. III B 1 above and discussed in Appendix H.

IV. MEASUREMENT OF THE SFF IN FLOQUET SYSTEMS

To study aspects of ergodicity, thermalization, and quantum chaotic dynamics, periodically driven or Floquet systems are particularly appealing for several reasons: First, due to the absence of energy conservation, generic Floquet systems can thermalize very rapidly and completely even for relatively small system sizes [50]. Further, since the density of quasienergies is generically flat, it is not necessary to unfold the spectra of Floquet systems to access their spectral statistics [45]. This relative simplicity of Floquet systems has led to intriguing recent results which, through explicit calculations of the SFF, establish an analytical connection between RMT and many-body quantum chaos in interacting periodically driven spin chains [30, 51–53]. As we discuss below, such Floquet spin models, and the experimental measurement of the SFF, can be realized naturally with Rydberg dressing schemes.

A. SFF of Floquet systems

In Floquet systems, we are interested in the statistics of eigenvalues of the unitary operator $U(\vartheta)$ which describes the evolution of the system during one driving period of duration ϑ : $U(\vartheta)|\ell\rangle = e^{-i\lambda_{\ell}\vartheta}|\ell\rangle$ with $\lambda_{\ell} \in [0, 2\pi/\vartheta]$ being the quasienergy. Similar to the Hamiltonian case [see Eq. (10)], we define the SFF for Floquet systems as [51]

$$K(t) = \overline{\left| \sum_{\ell} f_{\ell} e^{-i\lambda_{\ell}\vartheta t} \right|^2} = \overline{|\text{tr}[U(\vartheta)^t \rho_{\text{in}}]|^2}, \quad (15)$$

where the integer “time” t is the number of the evolution periods, $\rho_{\text{in}} = \sum_{\ell} f_{\ell} |\ell\rangle \langle \ell|$ is the initial quantum state, and the overline represents a possible average over disorder. Since generic interacting quantum chaotic Floquet systems exhibit a flat density of eigenstates in the thermodynamic limit, no spectral filtering or unfolding is necessary and one can use the infinite temperature ensemble $\rho_{\text{in}} = \rho_{\infty} = \mathcal{D}^{-1} \sum_{\ell} |\ell\rangle \langle \ell| \propto \mathbb{I}$ as the initial state (here \mathcal{D} is the dimension of the Hilbert space).

The behavior of the SFF in Floquet dynamics has the same characteristic features as in the Hamiltonian

case. As an illustration, below we consider two Floquet systems. First, we present a Floquet model which exhibits a crossover between the circular orthogonal ensemble (COE) and the circular unitary one (CUE) as a function of the driving frequency $\omega = 2\pi/\vartheta$ [54]. Then we consider kicked Ising models which demonstrate clear signatures of COE and CUE statistics even for a small system of $L = 4$ spins.

Crossover between COE and CUE statistics. – Here we consider an interesting example of a periodically driven system for which a random matrix class of the Floquet operator $U(\vartheta)$ differs from that of the time-dependent Hamiltonian $H(t)$ which generates the dynamics of the system [54]. To be specific, we consider a piecewise constant Hamiltonian with H_1 during the first half of the driving period and H_2 during the second half. The evolution operator over one period is of the form

$$U(\vartheta) = e^{-i(\vartheta/2)H_1} e^{-i(\vartheta/2)H_2}, \quad (16)$$

where H_1 and H_2 are Heisenberg Hamiltonians with random magnetic fields $h_i^{x,y,z}$, which are normally distributed around zero with unit variance,

$$H_1 = J \sum_i^L \left\{ \sum_{\eta=x,y,z} \sigma_i^\eta \sigma_{i+1}^\eta + \frac{1}{2} (h_i^x \sigma_i^x + h_i^y \sigma_i^y) \right\},$$

$$H_2 = J \sum_i^L \left\{ \sum_{\eta=x,y,z} \sigma_i^\eta \sigma_{i+1}^\eta + \frac{1}{2} (h_i^z \sigma_i^z - h_i^y \sigma_i^y) \right\}.$$

The Heisenberg models can be realized in the quantum simulator based on dressed Rydberg atoms as discussed in Sec. II. For generic values of the driving period ϑ the spectral statistics of the Floquet operator $U(\vartheta)$ is described by the CUE. However, for finite system sizes and in the limit of high driving frequencies, the dynamics of the system is described by an effective time-independent Hamiltonian $(H_1 + H_2)/2$ in which the random fields in the y direction cancel and time-reversal symmetry is restored. Therefore, in this limit, the spectral statistics of $U(\vartheta)$ belongs to the COE. We note that in this limit the density of quasienergies is determined by the effective Hamiltonian and is not flat. However, in the numerical examples below we find that effects due to a nonflat density of quasienergies are insignificant, and we take ρ_{in} in Eq. (15) to be the infinite temperature ensemble also for high driving frequencies.

The SFF and the simulated measurement of the SFF (see Sec. IV B below) are shown in Fig. (7). Remarkably, even the relatively small Floquet system of $L = 8$ spins exhibits clear RMT behavior with a crossover between COE and CUE statistics upon changing the Floquet period ϑ . In particular, we observe COE statistics for short periods or high driving frequencies (blue dots) with $\vartheta < \vartheta_c \sim 0.5/J$. The dot-dashed line shows the corresponding RMT prediction $K_{\text{COE}}(t) = [2t - t \ln(1 + 2t/\mathcal{D})] / \mathcal{D}^2$

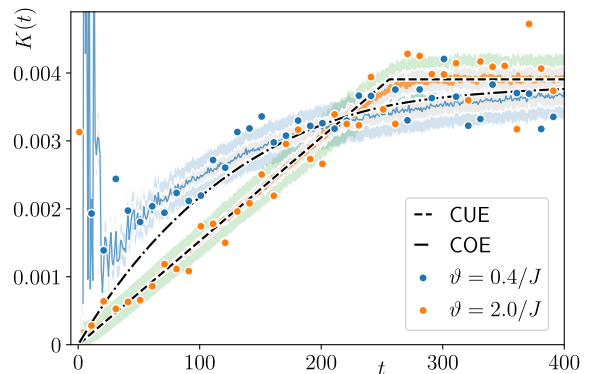


FIG. 7. Spectral form factor in the disordered Floquet model Eq. (16). The model exhibits a crossover between COE (blue dots) and CUE (orange dots) statistics as a function of the driving period ϑ . The black dashed and dot-dashed lines show the RMT predictions $K_{\text{CUE}}(t)$ and $K_{\text{COE}}(t)$, respectively. Numerical simulations are performed for $L = 8$ spins with 5×10^5 measurements per data point.

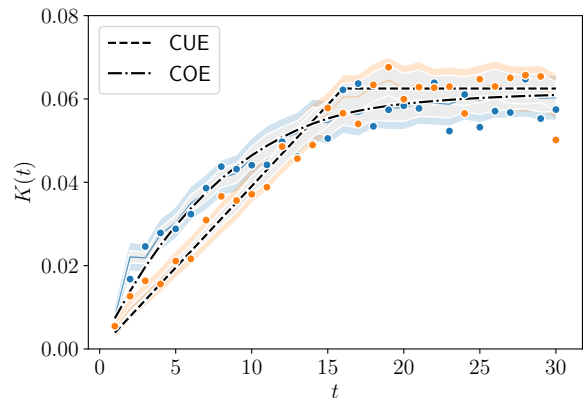


FIG. 8. Spectral form factor in the disordered kicked Ising models Eqs. (17), (18). Already in the small system of $L = 4$ spins the models exhibits a clear distinction between COE [$U_2(\vartheta)$ model shown with blue dots] and CUE [$U_3(\vartheta)$ model shown with orange dots] statistics. The black dashed and dot-dashed lines show the RMT predictions $K_{\text{CUE}}(t)$ and $K_{\text{COE}}(t)$, respectively. Numerical simulations are performed for 3.6×10^4 measurements per data point with driving period $\vartheta = 1/J$.

for $0 < t < \mathcal{D}$ where the Heisenberg time is set by the Hilbert space dimension $\mathcal{D} = 2^L$, see Eq. (12). For long periods $\vartheta > \vartheta_c$, the system is in the unitary class with CUE statistics (orange dots) resulting in $K_{\text{CUE}}(t) = t/\mathcal{D}^2$ for $0 < t < \mathcal{D}$ (dashed line), see also Eq. (13). We note that for sufficiently large values of ϑ the initial decay due to dephasing lasts at most a few driving cycles. This is because for these values of ϑ the unitary $U(\vartheta)$ is not a sparse matrix, as it is for $\vartheta \ll 1$, but a dense one coupling practically all states in the Hilbert space with each other. As a result, chaotic behavior starts already at $t = t_{\text{Th}} \sim 1$.

Small Floquet systems. – Now we consider two kicked

Ising models described by evolution operators

$$U_2(\vartheta) = e^{-iH_x\vartheta} e^{-iH_y\vartheta}, \quad (17)$$

$$U_3(\vartheta) = e^{-iH_x\vartheta} e^{-iH_y\vartheta} e^{-iH_z\vartheta}, \quad (18)$$

where $H_{x,y,z}$ are the transverse Ising Hamiltonians with random magnetic fields $h_i^{x,y,z} \in [-1, 1]$

$$H_x = J \sum_i^L (\sigma_i^x \sigma_{i+1}^x + h_i^y \sigma_i^y),$$

$$H_y = J \sum_i^L (\sigma_i^y \sigma_{i+1}^y + h_i^z \sigma_i^z),$$

$$H_z = J \sum_i^L (\sigma_i^z \sigma_{i+1}^z + h_i^x \sigma_i^x).$$

The two models described by the Floquet operators $U_2(\vartheta)$ and $U_3(\vartheta)$ belong to the COE and CUE random matrix classes, respectively. Remarkably, the statistical distinction can already be seen in a small system of $L = 4$ spins as the simulated measurement of the SFF shows in Fig. 8. In the quantum simulator based on Rydberg atoms the Ising models can be realized according to the general scheme presented in the Sec. II.

These examples illustrate that, as in the case of the Hamiltonian systems, the SFF provides a sensitive tool for probing quantum chaotic behavior of Floquet systems. At the same time, the measurement of the SFF in Floquet systems faces the same challenges as are present in Hamiltonian systems, i.e., small values of the signal and exponentially long time scales. However, for experimental studies of many-body quantum chaos, Floquet systems can be beneficial because they typically exhibit pronounced RMT behavior even for comparatively small system sizes. Moreover, since spectral filtering is not required in Floquet systems, the preparation step described in Sec. III B 1 can be omitted.

B. Measurement Protocol

To generalize the measurement protocol for the SFF in Hamiltonian systems described in Sec. III to Floquet systems, we reformulate it in terms of the unitary operator $\mathcal{U}(t)$ which describes the coupled evolution of the system and the control qubit during t Floquet periods of duration ϑ ,

$$\mathcal{U}(t) = U(\vartheta)^t \otimes |0\rangle_c \langle 0| + \mathbb{I} \otimes |1\rangle_c \langle 1|. \quad (19)$$

For simplicity, we focus here on Floquet systems with piecewise constant Hamiltonians H_k for time periods $\tau_{k-1} < \tau < \tau_k$, where $\tau_0 = 0$ and the time dependence is repeated periodically with period $\vartheta = \sum_k \tau_k$. The corresponding Floquet operator reads $U(\vartheta) = \prod_k e^{-i\tau_k H_k}$. The controlled evolution Eq. (19) is achieved by using

the QND interaction Hamiltonian (1) between the spin system and the control qubit with $H_{\text{spin}} \equiv H_k$:

$$\mathcal{U}(t) = \left[\prod_k e^{-i\tau_k H_k \otimes |0\rangle_c \langle 0|} \right]^t.$$

The measurement protocol for the SFF starts with the initialization of the control qubit in the state $|+\rangle$ and the system spins in the infinite temperature state ρ_∞ . (In practice, it is sufficient to sample from the infinite temperature ensemble by preparing the system, e.g., in random product states.) Then, for a particular realization of disorder in the instantaneous Hamiltonians H_k , we apply the controlled evolution $\mathcal{U}(t)$, and measure the expectation values of the operators σ_x and σ_y for the control qubit afterwards,

$$\begin{aligned} \langle \sigma^x(t) \rangle &= \text{Tr} \{ \mathcal{U}(t) \rho_\infty \otimes |+\rangle_c \langle +| \mathcal{U}(t)^\dagger \sigma^x \}, \\ &= \text{Re} \langle U(\vartheta)^t \rangle \\ \langle \sigma^y(t) \rangle &= \text{Im} \langle U(\vartheta)^t \rangle. \end{aligned}$$

Finally, the quantity $|\langle U(\vartheta)^t \rangle|^2 = \langle \sigma^x(t) \rangle^2 + \langle \sigma^y(t) \rangle^2$ is averaged over disorders realizations resulting in the SFF $K(t)$ for the Floquet system Eq. (15).

Experimental limitations of the measurement of the SFF in Floquet systems are analogous to the Hamiltonian case. As detailed in Sec. III B 2, these limitations originate from exponentially small values of the SFF in the presence of shot noise due to a finite number of experimental runs, as well as exponentially large values of \mathcal{D} , the analog of the Heisenberg time, and finite coherence times in real quantum simulators. As an example, the effect of a finite number of measurements is illustrated in the Figs. 7 and 8 for the Floquet system described by Eq. (16) and Eqs. (17), (18), respectively.

V. CONCLUSIONS AND OUTLOOK

Recent experimental studies of ergodicity breaking in quantum many-body systems focus on the absence of thermalization of local observables in integrable [55–57] and many-body localized systems [58–61], and on the slow growth of entanglement [61–63]. While it is firmly established through theoretical work that key signatures of ergodic vs. nonergodic dynamics are carried by individual eigenstates of the Hamiltonian of a quantum many-body system and the statistics of the corresponding eigenvalues, accessing these signatures in experiments requires novel approaches beyond the standard paradigm of quantum simulation. As a first main result of the present work, we have developed a method that enables in-depth experimental studies of the level statistics of interacting quantum many-body systems through the measurement of the SFF, and we have discussed the feasibility of observing the SFF signatures of ergodic (RMT) vs. non-ergodic dynamics for both disordered 1D Heisenberg and Floquet spin models. We conclude that the key features of RMT in the SFF

should be observable with presently available Rydberg experiments for system sizes of ten or more atoms. In a broader context, our method to measure the SFF is an example of a quantum protocol in which the state of a quantum simulator is prepared and monitored via the measurement of an auxiliary qubit, which is entangled with the quantum simulator by applying a QND gate. This is the second main result of our work: The implementation of a QND Hamiltonian $\mathcal{H}_{\text{QND}} = H_{\text{spin}} \otimes |0\rangle_c \langle 0|$ with Rydberg tweezer arrays, which yields a QND gate as $\mathcal{U}_{\text{QND}}(t) = e^{-i\mathcal{H}_{\text{QND}}t}$. In the context of a many-body system engineered with a Rydberg tweezer platform, this QND Hamiltonian can be implemented for a broad class of spin models specified by a Hamiltonian H_{spin} . While we consider 1D systems in form of a ring with the clock qubit in the center, our ideas also carry over to more complex 2D simulator geometries [1, 4, 36]. In addition, unique opportunities to combine quantum simulation with atomic clocks are offered by Alkaline Earth atoms [3, 64–66].

An intriguing possibility opened up by the present study is the design and implementation of more general quantum protocols involving QND gates entangling the quantum simulator with a freely designable H_{spin} with a set of control qubits. As noted before, this opens the door to run, for example, a quantum phase estimation algorithms on analog quantum simulators. In Ref. [67], a continuous readout of ‘the energy’ of a quantum many-body system was proposed as analog measurement of a homodyne current, with an implementation for a transverse Ising model with long range interaction. In contrast, quantum phase estimation based on the present QND gate with a freely designable H_{spin} provides an essentially universal, digital quantum algorithm to achieve measurement and preparation of (a narrow band of) energy eigenstates in an analog quantum simulator setting. Moreover, quantum phase estimation can be utilized to compute the dynamical response functions of quantum many-body systems [68]. This opportunity is of particular interest in the context of NMR, where the ability to design H_{spin} enables accessing the NMR spectra of molecules which are described by parametric Heisenberg models [69].

ACKNOWLEDGMENTS

The authors thank M. Lukin for helpful discussions. Work is supported by the European Union program Horizon 2020 under Grants Agreement No. 817482 (PASQuanS) and No. 731473 (QuantERA via QTFLAG), the US Air Force Office of Scientific Research (AFOSR) via IOE Grant No. FA9550-19-1-7044 LASCEM, by the Simons Collaboration on Ultra-Quantum Matter, which is a grant from the Simons Foundation (651440, P.Z.), and by the Institut für Quanteninformation. The parameters for the Rydberg simulations were obtained using the ARC library [Šibalić *et al.* [70]].

Appendix A: Dipole-dipole interactions

In this Appendix we provide details on the van der Waals interactions between $nP_{1/2} + nP_{1/2}$ and $nP_{1/2} + n'S_{1/2}$ states as relevant for the model of Sec. II. Our discussion adapts and extends Ref. [36].

For any pair of atoms i and j , the dipole-dipole interaction Hamiltonian reads [71]

$$V_{\text{dd}}^{(i,j)}(\vec{r}_{ij}) = \vec{d}^{(i)} \vec{d}^{(j)} / r_{ij}^3 - 3 \left(\vec{d}^{(i)} \vec{r}_{ij} \right) \left(\vec{d}^{(j)} \vec{r}_{ij} \right) / r_{ij}^5, \quad (\text{A1})$$

where $\vec{d}^{(i)}$ is the dipole operator of i -th atom and \vec{r}_{ij} is the relative distance between atoms. In second-order perturbation theory in $\hat{V}_{\text{dd}}^{(i,j)}$ we obtain the effective van der Waals interaction [36, 72] (we assume the absence of Förster resonances[44])

$$H_{\text{vdW}}^{(i,j)} \equiv P \sum_{\beta,\chi} \frac{V_{\text{dd}}^{(i,j)} Q_{\beta\chi} V_{\text{dd}}^{(i,j)}}{\delta_{\beta\chi}} P, \quad (\text{A2})$$

Here \hat{P} is the projector onto the states of interest ($nP_{1/2}$, $nP_{1/2}$ or $nP_{1/2}$, $n'S_{1/2}$), and $Q_{\beta\chi} \equiv |\beta, \chi\rangle \langle \beta, \chi|$ is the projector on manifolds that are populated only as virtual intermediate states, with $\delta_{\beta\chi}$ energy differences. We note that due to the perturbative nature of (A2), this expression is valid only beyond a certain critical radius $r > r_c$ (see below).

1. Interaction between simulator atoms

We first consider the van der Waals interaction between excited Rydberg states for the fine structure states $|r_{\alpha=\pm}\rangle = |nP_{1/2}, m_J = \pm 1/2\rangle$ of simulator atoms. The relevant projector reads

$$P = \sum_{\alpha=\pm} |r_{\alpha}\rangle_i \langle r_{\alpha}| \otimes \sum_{\alpha=\pm} |r_{\alpha}\rangle_j \langle r_{\alpha}|.$$

a)	$nP_{1/2} + nP_{1/2} \leftrightarrow n_{\beta}S_{1/2} + n_{\chi}S_{1/2}$
b)	$nP_{1/2} + nP_{1/2} \leftrightarrow n_{\beta}D_{3/2} + n_{\chi}D_{3/2}$
c)	$nP_{1/2} + nP_{1/2} \leftrightarrow n_{\beta}D_{3/2} + n_{\chi}S_{1/2}$
d)	$nP_{1/2} + nP_{1/2} \leftrightarrow n_{\beta}S_{1/2} + n_{\chi}D_{3/2}$

TABLE I. Channels of the dipole-dipole interaction of $nP_{1/2}$ Rydberg states.

The possible interaction channels for the atoms in $P_{1/2}$ states are listed in Table I, which provides us with the intermediate states $|\beta, \chi\rangle$ of Eq. (A2). This allows us to write the matrix of van der Waals interaction Hamiltonian $H_{\text{vdW}}^{(i,j)}$ in the form (7) [43] with $C_6 = 2 \left[C_6^{(a)} + 4C_6^{(b)} + 2 \left(C_6^{(c)} + C_6^{(d)} \right) \right] / 27$ and $\tilde{C}_6 =$

$C_6^{(a)} + C_6^{(b)} - C_6^{(c)} - C_6^{(d)}$ combinations of coefficients $C_6^{(a,b,c,d)}$ attributed to different scattering channels. (Explicit expressions involving Clebsch-Gordan and dipole matrix elements can be found in [36, 72]), and corresponding plots for Rb atoms are shown in Fig. 9(a). The 4×4 matrix $\mathbb{D}_0(\theta, \phi)$ referred to in Eq. (7) reads

$$\mathbb{D}_0(\theta, \phi) = \begin{pmatrix} \frac{3 \cos(2\theta) - 1}{81} & \frac{4e^{-i\phi} \sin(2\theta)}{27} & \frac{4e^{-i\phi} \sin(2\theta)}{27} & \frac{2e^{-2i\phi} \sin^2(\theta)}{27} \\ \frac{e^{i\phi} \sin(2\theta)}{27} & \frac{1 - 3 \cos(2\theta)}{81} & \frac{-5 - 3 \cos(2\theta)}{81} & \frac{-4e^{-i\phi} \sin(2\theta)}{27} \\ \frac{e^{i\phi} \sin(2\theta)}{27} & \frac{-5 - 3 \cos(2\theta)}{81} & \frac{1 - 3 \cos(2\theta)}{81} & \frac{-4e^{-i\phi} \sin(2\theta)}{27} \\ \frac{2e^{2i\phi} \sin^2(\theta)}{27} & \frac{-4e^{i\phi} \sin(2\theta)}{27} & \frac{-4e^{i\phi} \sin(2\theta)}{27} & \frac{3 \cos(2\theta) - 1}{81} \end{pmatrix},$$

and following the geometry of our setup in Fig. 1(b) we set $\theta = \pi/2$. Thus we obtain for the interaction Hamiltonian the structure

$$V_{\text{vdW}}^{(i,j)} = \begin{pmatrix} W_{++}^{(i,j)} & 0 & 0 & V_{++}^{(i,j)} \\ 0 & W_{+-}^{(i,j)} & V_{+-}^{(i,j)} & 0 \\ 0 & V_{+-}^{(i,j)} & W_{-+}^{(i,j)} & 0 \\ V_{--}^{(i,j)} & 0 & 0 & W_{--}^{(i,j)} \end{pmatrix}, \quad (\text{A3})$$

where

$$W_{++}^{(i,j)} = W_{--}^{(i,j)} = \frac{1}{r_{ij}^6} [C_6 - \frac{4}{81} \tilde{C}_6],$$

$$W_{+-}^{(i,j)} = W_{-+}^{(i,j)} = \frac{1}{r_{ij}^6} [C_6 + \frac{4}{81} \tilde{C}_6],$$

$$V_{+-}^{(i,j)} = V_{-+}^{(i,j)} = -\frac{2}{81} \frac{\tilde{C}_6}{r_{ij}^6},$$

and

$$V_{++}^{(i,j)} = V_{--}^{(i,j)*} = -\frac{2}{27} \frac{\tilde{C}_6}{r_{ij}^6} \exp(-2i\phi). \quad (\text{A4})$$

The specific spin models which can be engineered via Rydberg dressing [36, 37], i.e. by admixing the van der Waals interactions (A3) to the ground states by off-resonant laser light, is determined by the structure of the matrix elements (A4).

2. Interactions between simulator and control atoms

Here we consider the van der Waals interaction between the simulator and control atoms in the Rydberg states. We restrict the states of the control atom to the Zeeman manifold which includes the logical qubit state $|1\rangle_c$, i.e. $|1\rangle_c = |n'S_{1/2}, m_j = 1/2\rangle$, and $|1'\rangle_c \equiv$

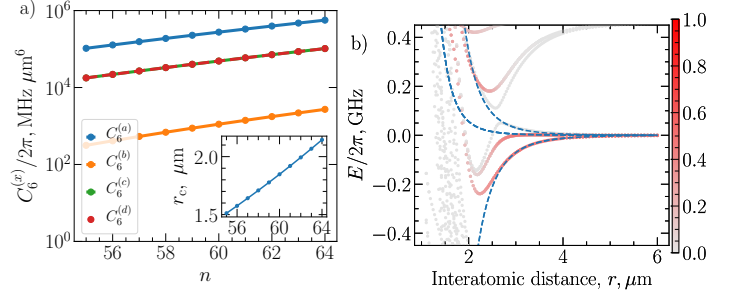


FIG. 9. Van der Waals interaction of two $nP_{1/2}$ Rydberg states. (a) $C_6^{(x)}$ coefficient as function of the principal quantum number n . Inset shows the critical radius r_c . (b) Exact diagonalization of dipole-dipole interaction. Color indicates the projection of exact eigenstates onto the state $|r_+\rangle_i |r_+\rangle_j$. Blue dashed line stands for the eigenvalues of the perturbative Hamiltonian Eq. (A3).

$|n'S_{1/2}, m_j = -1/2\rangle$. As we discussed below, the unwanted coupling between $|1\rangle_c$ and $|1'\rangle_c$ can be minimized by proper choice of the principal quantum number n' [43]. For the states of simulator atoms we again consider $|r_{\alpha=\pm}\rangle = |nP_{1/2}, m_J = \pm 1/2\rangle$.

a)	$nP_{1/2} + n'S_{1/2} \leftrightarrow n_\beta S_{1/2} + n_\chi P_{1/2}$
b)	$nP_{1/2} + n'S_{1/2} \leftrightarrow n_\beta D_{3/2} + n_\chi P_{3/2}$
c)	$nP_{1/2} + n'S_{1/2} \leftrightarrow n_\beta D_{3/2} + n_\chi P_{1/2}$
d)	$nP_{1/2} + n'S_{1/2} \leftrightarrow n_\beta S_{1/2} + n_\chi D_{3/2}$

TABLE II. Channels of the dipole-dipole interaction of $nP_{1/2}, n'S_{1/2}$ Rydberg states.

The relevant scattering channels are listed in Table II. Similar to (A1) above, we obtain for $H_{\text{vdW}}^{(i,c)}$ in the basis $(|r_+\rangle |1\rangle_c, |r_+\rangle |1'\rangle_c, |r_-\rangle |1\rangle_c, |r_-\rangle |1'\rangle_c)$ an expression analogous to Eq. (7),

$$V_{\text{vdW}}^{(i,c)} = \frac{1}{r_{i,c}^6} \left[C'_6 \mathbb{I}_4 - \tilde{C}'_6 \mathbb{D}_0(\theta, \phi) \right], \quad (\text{A5})$$

where coefficients C'_6 and \tilde{C}'_6 are defined as above. Numerical results for C'_6 , and the relative strength of the second (anisotropic) term in Eq. (A5) are shown in Figs. 10(a,b), respectively, for different principle quantum numbers n and $n' = n + \Delta n$. As can be seen from Fig. 10(b), the second term in $V_{\text{vdW}}^{(i,c)}$ can be made much smaller than the first one by choosing n and Δn properly. This makes the interaction essentially isotropic.

We note, however, that, even when the condition $|\tilde{C}'_6| \ll |C'_6|$ is satisfied, the second term in Eq. (A5) may cause unwanted transitions between the Rydberg states of the control atom, $|1\rangle_c \leftrightarrow |1'\rangle_c$, which can bring the control atom out of the Hilbert space of interest. To suppress such transitions, we make them strongly off-resonant by

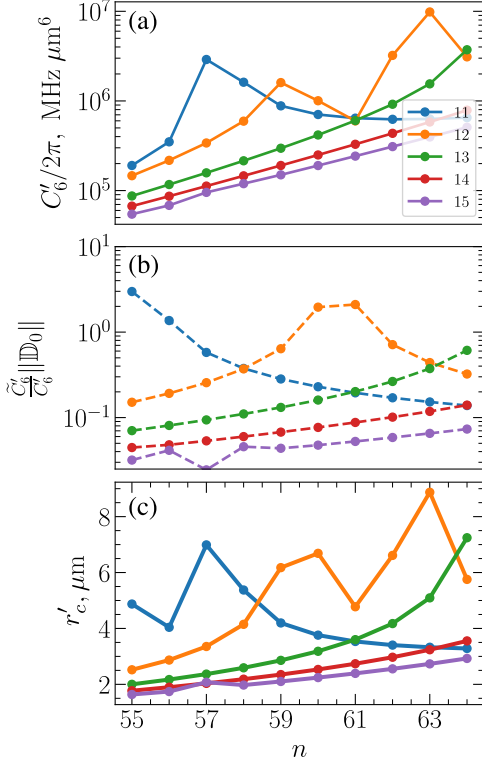


FIG. 10. Van der Waals interaction between the Rydberg states of the simulator and control atoms with the principle quantum numbers n and $n' = n + \Delta n$, respectively (Δn is shown in different colors as indicated on the inset). (a) C_6' coefficient as a function of n for different values of Δn . (b) Relative strength of two contribution to $V_{\text{vdW}}^{(i,c)}$ with $\|\mathbb{D}_0\| = 2\sqrt{2}/27$ being the Frobenius norm of the matrix \mathbb{D}_0 . (c) Critical distance r'_c for the van der Waals interaction between simulator and control atoms, see text.

imposing e.g. an external magnetic field. Thus we assume that the Hilbert space of the control atom can be represented by the two qubit states $|0\rangle_c$ and $|1\rangle_c$, and we can describe the interaction between the simulator atom and the control qubit by the ‘blockade’ Hamiltonian (8).

3. Validity of the van der Waals Hamiltonian

Before proceeding, we emphasize that the validity of the van der Waals interaction Hamiltonian Eq. (A2) requires the conditions [71, 73] to be satisfied:

$$\begin{aligned} \max_{\beta\chi} \left\{ i \langle r_{\pm} | j \langle r_{\pm} | V_{dd}^{(i,j)} \delta_{\beta\chi}^{-2} Q_{\beta\chi} V_{dd}^{(i,j)} | r_{\pm} \rangle_i | r_{\pm} \rangle_j \right\} &\ll 1, \\ \max_{\beta\chi} \left\{ c \langle 1 | i \langle r_{\pm} | V_{dd}^{(i,j)} \delta_{\beta\chi}^{-2} Q_{\beta\chi} V_{dd}^{(i,j)} | r_{\pm} \rangle_i | 1 \rangle_c \right\} &\ll 1 \end{aligned}$$

which sets the lower bound on the interatomic distance, $r_{ij} > r_c$, for $i, j = 1, \dots, L$, and $r_{i,c} > r'_c$, where the

critical distances r_c and r'_c are defined as the distances when the left-hand-side in the above condition equals unity. The calculated dependencies of r_c and r'_c on the main quantum numbers are shown in the inset of Fig. 9(a) and in Fig. 10(c), respectively. For the simulator atoms, however, direct diagonalization of $V_{dd}^{(i,j)}$, Eq. (A1), shows the presence of an avoided crossing at $r_{ij} \approx 2.4\mu\text{m}$, see Fig. 9(b). Therefore, to stay away from this nonperturbative situation, we take $r_c = 2.4\mu\text{m}$ and (using $n = 60$ and $n' = 71$ as principal quantum numbers) for the shortest interatomic distances in our setup.

Appendix B: Derivation of the effective Hamiltonian

In this Appendix we derive the effective Hamiltonian of the simulator-qubit interaction which we show to be given by Eq. (9). We perform an adiabatic elimination of excited Rydberg states of simulator atoms $|r_{\pm}\rangle$ following [36]. We first transform Hamiltonian H_s [see Eqs. (4)-(6)] into rotating frame:

$$H_s = \sum_{i=1}^L H_0^{(i)} + \sum_{i,j=1}^L H_{\text{vdW}}^{(i,j)}, \quad (\text{B1})$$

where

$$\begin{aligned} H_0^{(i)} &= \sum_{\alpha=\pm} (\Omega_{\alpha} |g_{\alpha}\rangle \langle g_{\alpha}| + \text{H.c.}) \\ &\quad - \Delta_B (|r_{-}\rangle_i \langle r_{-}| + |g_{-}\rangle_i \langle g_{-}|) \\ &\quad - \sum_{\alpha=\pm} \Delta_{\alpha} |r_{\alpha}\rangle_i \langle r_{\alpha}|, \end{aligned} \quad (\text{B2})$$

and $\Delta_B = \omega_{+} - \omega_{-} + E_{g_{+}} - E_{g_{-}}$, $\Delta_{\pm} = E_{r_{\pm}} - E_{g_{\pm}} - \omega_{\pm}$. The explicit expression of van der Waals interaction Hamiltonian according to Eq. (A3) is

$$\begin{aligned} H_{\text{vdW}}^{(i,j)} &= \sum_{\alpha,\alpha'} W_{\alpha\alpha'}^{(i,j)} |r_{\alpha}\rangle_i \langle r_{\alpha}| \otimes |r_{\alpha'}\rangle_j \langle r_{\alpha'}| \\ &\quad + V_{+-}^{(i,j)} |r_{+}\rangle_i \langle r_{-}| \otimes |r_{-}\rangle_j \langle r_{+}| + \text{H.c.} \\ &\quad + V_{--}^{(i,j)} |r_{+}\rangle_i \langle r_{-}| \otimes |r_{+}\rangle_j \langle r_{-}| + \text{H.c.}, \end{aligned}$$

We now define the dressed ground $|\tilde{g}_{\alpha}\rangle_i$ and Rydberg $|\tilde{r}_{\alpha}\rangle_i$ states as the eigenstates of the Hamiltonian $H_0^{(i)}$,

$$\begin{aligned} |\tilde{g}_{\alpha}\rangle_i &= \frac{\sqrt{\lambda_{-}} |g_{\alpha}\rangle_i - \sqrt{\lambda_{+}} |r_{\alpha}\rangle_i}{\sqrt{\lambda_{+} + \lambda_{-}}}, \\ |\tilde{r}_{\alpha}\rangle_i &= \frac{\sqrt{\lambda_{+}} |g_{\alpha}\rangle_i + \sqrt{\lambda_{-}} |r_{\alpha}\rangle_i}{\sqrt{\lambda_{+} + \lambda_{-}}}, \end{aligned} \quad (\text{B3})$$

where $\lambda_{\pm} = [(\Delta_{\alpha}/2)^2 + \Omega_{\alpha}^2]^{1/2} \pm \Delta_{\alpha}/2$ (we assume $\Delta_{\alpha} > 0$ and real Rabi frequencies Ω_{α}).

We now define the projectors onto the subspace of the dressed ground states $|\tilde{g}_\alpha\rangle_i$

$$P_g = \bigotimes_{i=1}^L \left(\sum_{\alpha=\pm} |\tilde{g}_\alpha\rangle_i \langle \tilde{g}_\alpha| \right) \quad (\text{B4})$$

and $Q = \bigotimes_{i=1}^L \mathbb{I}_i - P_g$. Equivalently, we can write P_g as a sum of projectors onto the eigenstates of the Hamilto-

nian $\sum_i H_0^{(i)}$ with the eigenenergy $E_l^{(0)}$, $P_g = \sum_l P_g^{(l)}$, where $P_g^{(l)}$ is the projector onto the subspace formed by the eigenstate with the eigenenergy $E_l^{(0)}$. Due to the particular form of the blockade interaction Eq. (A5) we can perform the adiabatic elimination of excited states simultaneously for the two states of the qubit. We now derive the effective Hamiltonian of the simulator atoms using projectors, and write an effective Hamiltonian in the P_g subspace up to two lowest orders in V as [74]

$$H_{\text{eff}} = P_g H_s P_g + \frac{1}{2} \left\{ P_g H_s Q \sum_l \left(E_l^{(0)} - Q H_s Q \right)^{-1} Q H_s P_g^{(l)} + \text{H.c.} \right\}. \quad (\text{B5})$$

After evaluating this expression analytically up to the 4-th order in $\xi_\alpha \equiv \Omega_\alpha/\Delta_\alpha$, we obtain [36] the effective Hamiltonian in general XYZ form:

$$H_{\text{eff}}(\Delta_\alpha) = \sum_{i<j=1}^L \sum_{\eta=x,y,z} J_{ij}^{(\eta)}(\Delta_\alpha) \sigma_i^\eta \sigma_j^\eta + \sum_{i=1}^L \left[h^z(\Delta_\alpha) + \frac{1}{2} \Delta_B \right] \sigma_i^z, \quad (\text{B6})$$

We now show that the model can be reduced to the Heisenberg XXZ model assumed in the main text, and provide the corresponding interaction coefficients $J_{ij}^{(\eta)}$, h^z . The expressions for the Hamiltonians H_{spin} and H'_{spin} in Eq. (9) are

$$H_{\text{spin}} = H_{\text{eff}}(\Delta_\alpha), \quad (\text{B7})$$

$$H'_{\text{spin}} = H_{\text{eff}}(\Delta_\alpha - C'_6/R^6) \quad (\text{B8})$$

As a result of the adiabatic elimination procedure the qubit logical states $|0\rangle_c$ and $|1\rangle_c$ respectively acquire additional spin-independent shifts $\sum \beta_{ij}$ and $\sum \beta'_{ij}$ (see below). Thus in the rotating frame of the control laser frequency, the Hamiltonian takes on the form Eq. (9) with an effective detuning $\delta = \sum_{ij} (\beta'_{ij} - \beta_{ij}) + E_{\text{cr}} - E_{\text{cg}}$.

We now discuss the effective Hamiltonians (B7) and (B8). In the case of a perfect blockade, $C'_6/(\Delta_\alpha R^6) \rightarrow \infty$, one has $J_{ij}^{(\eta)}(\Delta_\alpha - C'_6/R^6) \rightarrow 0$ and $h_i^z(\Delta_\alpha - C'_6/R^6) \rightarrow 0$ and, therefore, H'_{spin} reduces to a simple form $H'_{\text{spin}} = (1/2)\Delta_B \sum_{i=1}^L \sigma_i^z$. With this we are able to identify two regimes when the Hamiltonian Eq. (9) gives rise to the desired QND Hamiltonian, i.e. $[H_{\text{spin}}, H'_{\text{spin}}] = 0$. The first one corresponds to $\Delta_B = 0$. In this manuscript we focus on the second regime of a ‘‘strong magnetic field’’ when $\Delta_B \rightarrow \infty$ (more precisely, $|\Delta_B| \gg |J_{ij}^{(\eta)}|, |h_i^z|$) when the spin model effectively reduces to the Heisenberg XXZ chain. The explicit expressions for the couplings are then given by

$$h^z = 0, \quad (\text{B9})$$

$$J_{ij}^{(x,y)} = -2\Delta^2 \xi^4 \frac{V_{+-}^{(i,j)}}{\left(V_{+-}^{(i,j)} - W_{+-}^{(i,j)} - 2\Delta \right) \left(2\Delta + V_{+-}^{(i,j)} + W_{+-}^{(i,j)} \right)}, \quad (\text{B10})$$

$$J_{ij}^{(z)} = -2\Delta^2 \xi^4 \frac{V_{+-}^2 - \left(2\Delta + W_{+-}^{(i,j)} \right) \left(W_{+-}^{(i,j)} - W_{++}^{(i,j)} \right)}{\left(2\Delta + W_{+-}^{(i,j)} \right) \left(V_{+-}^{(i,j)} - W_{+-}^{(i,j)} - 2\Delta \right) \left(2\Delta + V_{+-}^{(i,j)} + W_{+-}^{(i,j)} \right)}, \quad (\text{B11})$$

$$\beta_{ij} = -2\Delta \xi^2 + 2\Delta \xi^4 \frac{V_{+-}^2 \left(3\Delta + 2W_{++}^{(i,j)} \right) - \left(2\Delta + W_{+-}^{(i,j)} \right) \left[4\Delta^2 + 3\Delta \left(W_{+-}^{(i,j)} + W_{++}^{(i,j)} \right) + 2W_{+-}^{(i,j)} W_{++}^{(i,j)} \right]}{\left(2\Delta + W_{+-}^{(i,j)} \right) \left(V_{+-}^{(i,j)} - 2\Delta - W_{+-}^{(i,j)} \right) \left(2\Delta + V_{+-}^{(i,j)} + W_{+-}^{(i,j)} \right)} \quad (\text{B12})$$

where V and W refer to the van der Waals interaction

derived in (A1), and we assumed equal Rabi frequencies

and detunings, such that $\xi_\alpha = \xi$. If the energy difference between the subspaces is much larger than the coupling $|J_{ij}^{(\eta)}| \ll |\Delta_B|$, this term can be neglected, such that the resulting low-energy dynamics (with typical energies $\sim J$) takes place in a the sector with a fixed $S_z = \sum_i \sigma_i^z$.

To conclude, we note that in Eq. (B6) one can also generate a *position-dependent* magnetic field, $h^z \rightarrow h_i^z = h^z + \delta h_i^z$. This can be achieved by using position dependent Rabi frequencies, $\Omega_\alpha^{(i)} = \Omega_\alpha + \delta\Omega_\alpha^{(i)}$, which results in $\delta h_i^z \approx \sum_\alpha \alpha \xi_\alpha \delta\Omega_\alpha^{(i)}$. After choosing $\delta\Omega_\alpha^{(i)} \sim (J/\xi)w_i$, where $w_i \in [-1, 1]$ is a uniformly distributed random number, we obtain $\delta h_i^z \sim J$.

Appendix C: Implementation of complex flip-flop phases

We now provide a way to engineer *complex* flip-flop coefficients in our spin models. As a starting point, let us consider the dressing lasers with the Laguerre-Gaussian spatial mode profile corresponding to the angular momentum l_\pm (note that it is sufficient to have only one nonzero l_α). In this case, the dressing term in the Hamiltonian Eq. (4) becomes

$$\sum_{k=1}^L \sum_{\alpha=\pm} (\Omega_\alpha^{\text{LG}} e^{i\phi_{k,\alpha}} |g_\alpha\rangle_k \langle r_\alpha| e^{i\omega_\alpha t} + \text{H.c.}), \quad (\text{C1})$$

where $\phi_{k,\pm} \equiv 2\pi k l_\pm / L$. After performing the adiabatic elimination procedure as in Sec. B of this Appendix, we obtain the effective Hamiltonian of the form following form (we omit here the Δ_B -term)

$$\begin{aligned} H_{\text{eff}}(\tilde{\Delta}_\alpha) &= \sum_{i < j=1}^L \left\{ 2J_{kj}^{(x,y)} \left(e^{i\sum_\alpha \alpha(\phi_{k,\alpha} - \phi_{j,\alpha})} \sigma_k^+ \sigma_j^- + \text{H.c.} \right) \right\} \\ &+ \sum_{i < j=1}^L \left\{ J_{kj}^{(z)} \sigma_k^z \sigma_j^z \right\} + \sum_{i=1}^L h_i^z \sigma_i^z, \end{aligned} \quad (\text{C2})$$

with the flip-flop amplitudes acquiring nonzero phases $\phi_{kj} = i \sum_\alpha \alpha(\phi_{k,\alpha} - \phi_{j,\alpha})$. We note, however, that the sum of the flip-flop phases in Eq. (C2) across the system is always equal to an integer number of 2π , having, therefore, no effect on spectral statistics. However, physically relevant phase of the flip-flop amplitudes can be generated using stroboscopic engineering. Let us consider the case when, during the stroboscopic period $T = 2\pi/\omega_s$, we use the plane-wave dressing lasers with the Rabi frequencies Ω_α for the time $0 \leq t_1 \leq T$, and the Laguerre-Gaussian dressing lasers with the Rabi frequencies $\Omega_\alpha^{\text{LG}}$ for the time $t_2 = T - t_1$. Then, for the stroboscopic frequency satisfying the condition $h, J \ll \omega_s \ll \Delta_\pm$, the effective

Rabi frequencies at the atomic positions are

$$\Omega_{\alpha,k}^{\text{eff}} = \frac{1}{T} (t_1 \Omega_\alpha + t_2 \Omega_\alpha^{\text{LG}} e^{i\phi_{k,\alpha}}) = |\Omega_\alpha^{\text{eff}}| e^{i\phi_{k,\alpha}^{\text{eff}}}, \quad (\text{C3})$$

where

$$|\Omega_\alpha^{\text{eff}}| = \frac{1}{T^2} [(t_1 \Omega_\alpha + t_2 \Omega_\alpha^{\text{LG}} \cos \phi_{k,\alpha})^2 + (t_2 \Omega_\alpha^{\text{LG}} \sin \phi_{k,\alpha})^2]^{1/2}$$

and

$$\tan \phi_{k,\alpha}^{\text{eff}} = \frac{\sin \phi_{k,\alpha}}{\cos \phi_{k,\alpha} + t_1/t_2}.$$

We see that, by varying the ratio t_1/t_2 , one can generate values $\phi_{k,\alpha}^{\text{eff}} \in [0, \phi_{k,\alpha}]$ for the effective phases. With the effective Rabi frequencies (C3), the resulting phases of the flip-flop terms are not multiples of 2π anymore, and the corresponding Hamiltonian (C2) belongs now to the unitary ensemble.

Appendix D: Experimental considerations for SFF

In this Appendix we discuss in more details the experimental challenges of the SFF protocol, which limit the achievable system sizes. We also present estimations of the coherence times and the available system sizes for our Rydberg tweezer implementation.

Time scales: – Propagation up to the Heisenberg time $\tau_H \sim 2^L/JL$ is limited by the finite coherence time of the quantum simulator. First, the preparation time (with M measurements) is $t_{\text{prep}} \approx t_0 2^M \leq \pi(JL)^{-1} 2^{M-1}$ (see Sec. III B 1). Therefore, the lower bound on the coherence time is $t_{\text{coh}} > t_{\text{prep}} \approx (JL)^{-1} 2^{M-1}$. Observation of the behavior of $K(\tau)$ at times $\tau \sim \tau_H$, requires coherence times $t_{\text{coh}} > \tau_H \sim (JL)^{-1} 2^L$. In the case of a dominant individual single-spin decoherence with the dephasing rate γ_d , the corresponding condition reads $J/\gamma_d > 2^L$. This limits observation of $K(\tau)$ at times $\tau \sim \tau_H$ to moderate system sizes (see estimates for the Rydberg tweezer array below). We note, however, that, even when the Heisenberg time τ_H is not accessible, the transition to chaotic dynamics at the Thouless time τ_{Th} and the distinct behaviors of the SFF for quantum chaotic [$K(\tau) \sim \tau$] and integrable systems [$K(\tau) \sim \text{const}$] takes place at much shorter times to be compared with t_{coh} . In general, systems with smaller L are characterized by shorter characteristic times, and require fewer experimental runs to resolve the key features (see discussion below). On the other hand, finite size effects tend to wash out the characteristic features of $K(\tau)$ signaling the chaotic behavior.

Signal magnitude: – The scaling of typical SFF values can be estimated as $K_\infty \sim N_{\Delta E}^{-1}$ for the late time plateau value and as $K(\tau \approx \tau_{\text{Th}}) \sim N_{\Delta E}^{-3/2}$ [75] for the SFF minimum preceding the Thouless time τ_{Th} , here $N_{\Delta E} \gg 1$ is the number of eigenstates in the initial MC ensemble ρ_{mc} . Preparation of MC ensemble (see Sec. III B 1) using M filtering steps (control qubits) produces ρ_{mc} with $N_{\Delta E} \sim 2^{L-M}$ eigenstates. Since the

protocol has a success probability $p_{\text{mc}} \sim 2^{-M}$ and the QND measurement scheme can exploit the prepared state several times (N_{reuse}) one can perform N measurements per data point in $N_{\text{run}}^{(1)} \simeq N/(p_{\text{mc}}N_{\text{reuse}})$ experimental runs per one disorder realization. On the other hand, the threshold signal level which can be distinguished from the shot noise after averaging over N_d realizations of disorder in the spin Hamiltonian and N measurements per one disorder is given by $K_* \sim 1/(N\sqrt{N_d})$ (Appendix F). We find the necessary number of measurements using the condition $K_* \sim K_\infty$. Thus, the number of experimental runs $N_{\text{run}} = N_d N_{\text{run}}^{(1)}$ per data point necessary to resolve the features of interest in $K(\tau)$, is given by $N_{\text{run}} > 2^L \sqrt{N_d}/N_{\text{reuse}}$.

The number of filtering steps M does not affect N_{run} for the probabilistic preparation scheme, therefore, it is enough to use $M \sim 3$ to eliminate the contribution of spectral edges in the SFF. However, it might be possible to use a semi-deterministic preparation scheme, e.g., by populating excited energy eigenstates in some energy interval by driving or quenching the system [33] followed by verification via M filtering steps with high probability (~ 1) of success. In this case, the necessary number of experimental runs per data point can be improved $N_{\text{run}} > 2^{L-M}$.

Rydberg tweezer implementation: – We conclude with a discussion of imperfections for the Rydberg tweezer implementation, in particular decoherence rates and the effectiveness of the Rydberg blockade. We also elaborate on geometrical limitations on interatomic distances which ensure the validity of our Rydberg dressing and put a constraint on the maximal size of the system.

We start with the discussion of the decoherence effects which limit the duration of the experiment. They originate from the finite lifetime of the Rydberg atomic states and from the error rate in the gate operation caused by non-perfect Rydberg blockade mechanism (the term with H'_{spin} in (9)). The former is characterized by two dimensionless parameters $\kappa_1 \equiv \gamma'_d/|H_{\text{spin}}| \sim \gamma'_d/(JL)$ and $\kappa_2 \equiv \xi_\pm^2 \gamma_d L/|H_{\text{spin}}| \sim \xi_\pm^2 \gamma_d/J$, for the control atom and the spin system, respectively. Here γ'_d and γ_d are the spontaneous emission rates for the corresponding Rydberg states, and for the system atoms we take into account the collective enhancement ($\sim L$) of the spontaneous emission rate due to highly entangled nature of the many-body excited states. The factor ξ_\pm^2 in κ_2 represents the admixture of the Rydberg state as a result of the dressing. In a similar way, the error rate in the gate operation can be quantified by the parameter $\kappa_3 \equiv |H'_{\text{spin}}|/|H_{\text{spin}}|$ which can be estimated [see Eqs. (B10) and (B11)] as $\kappa_3 \sim (R/R_b)^{24}$ for $R < R_b$, where R is the distance between the control atom and the system atoms and $R_b \equiv \sqrt[6]{C'_6/\Delta_\pm}$ is the Rydberg blockade radius with C'_6 being the interaction constant [see Eq. (8)]. We note here the very high power in the above estimate such that κ_3 decreases very rapidly for $R < R_b$, giving, for example, $\kappa_3 \sim 10^{-3}$ for $R/R_b = 0.8$. The largest of these parameters $\kappa = \max\{\kappa_i\}$ sets the upper bound for the

time during which the evolution is coherent and follows the ideal QND Hamiltonian (1), $t_{\text{coh}} \sim (JL\kappa)^{-1}$.

As an example let us consider the Rydberg states with $n' = 71$ (control atom) $n = 60$ (system atom) and the following parameters of the dressing scheme: $\Delta_\pm = -9$ MHz and $\xi_\pm = 0.2$. The decoherence rates for the atoms are $\gamma_d \approx 2\pi \times 318$ Hz, $\gamma'_d \approx 2\pi \times 406$ Hz. The parameters characterizing the spontaneous emission are then $\kappa_1 \approx 4.4 \cdot 10^{-4}$, $\kappa_2 = 1.6 \cdot 10^{-4}$ for $L \sim 10$ atoms and the Rydberg blockade radius is $R_b \approx 6.5 \mu\text{m}$ (see Fig. 10). For κ_3 to be of the same order or smaller, one should have $R \sim R_{\text{max}} = 0.75 R_b \approx 5 \mu\text{m}$ as an upper bound on the distance between the system and control atoms. In our system κ_3 is the largest decoherence parameter and it limits the coherence times to $t_{\text{coh}} \sim 10^2 J^{-1}$.

The constraint on the distance between the system atoms is related to the validity of our dressing scheme which is to say the validity of the perturbative approach: It has to be larger than some minimal value, $R_{ij} > r_c = 2.4 \mu\text{m}$, see Appendix A 2. Within our ring setup [see Fig. 1(b)] in which the radius is given by R_{max} and the separation between system atoms is limited by r_c , simple geometrical considerations give the maximal number of system atoms which is with both constraints, $L_{\text{max}} \simeq \pi/\arcsin[r_c/(2R_{\text{max}})] = 12$, the number used in our numerical simulations.

Appendix E: Preparation of a microcanonical ensemble

In this Appendix we present detailed description of the preparation of microcanonical ensembles via low resolution PEA as discussed in Sec. III B 1. As explained in the main text the preparation procedure involves M rounds of the QND interaction entangling the spin system and the control qubit according to $\mathcal{U}(t_m, \delta) = \exp\{-i[(H_{\text{spin}} - \delta) \otimes |0\rangle\langle 0|] t_m\}$ followed by qubit measurements.

After the entanglement, the measurement of the control qubit with a measurement outcome $v_m = \{\pm\}$ collapses a state ρ of the spin system into a conditional (unnormalized) state

$$\rho \rightarrow \mathcal{M}(v_m, t_m, \delta) \rho \mathcal{M}^\dagger(v_m, t_m, \delta),$$

where the measurement operators $\mathcal{M}(\pm, t, \delta) = \langle \pm | \mathcal{U}(t, \delta) | + \rangle$ act in the system Hilbert space and have a diagonal representation in the energy eigenbasis

$$\mathcal{M}(+, t, \delta) = \sum_{\ell} e^{-i(E_\ell - \delta)t/2} \cos[(E_\ell - \delta)t/2] |\ell\rangle \langle \ell|, \quad (\text{E1})$$

$$\mathcal{M}(-, t, \delta) = i \sum_{\ell} e^{-i(E_\ell - \delta)t/2} \sin[(E_\ell - \delta)t/2] |\ell\rangle \langle \ell|. \quad (\text{E2})$$

The full sequence of control qubit measurements with outcomes $\vec{v} \equiv \{v_m\}$ defines the resulting unnormalized state of the spin system

$$\tilde{\rho}_{\text{out}} = \mathbb{M}(\vec{v}, \delta) \rho_{\text{in}} \mathbb{M}^\dagger(\vec{v}, \delta),$$

where $\mathbb{M}(\vec{v}, \delta) = \prod_{m=0}^{M-1} \mathcal{M}(v_m, t_m, \delta)$. As a result, the unnormalized probability p_ℓ for the eigenstates $|\ell\rangle$ with the eigenenergy E_ℓ to appear in ρ_{out} is

$$p_\ell = \langle \ell | \tilde{\rho}_{\text{out}} | \ell \rangle = P(\vec{v}, E_\ell - \delta) \langle \ell | \rho_{\text{in}} | \ell \rangle,$$

$$P(\vec{v}, x) = \prod_{m=0}^{M-1} P_m(v_m, x),$$

where $P_m(\pm, x) = \{1 \pm \cos(xt_m)\}/2$.

If we now select a run with all readouts “+”, $v_m = \{+\}$, $m = 0, \dots, M-1$, we obtain the output state with the narrow energy distribution

$$p_\ell = P(+_0, \dots, +_{M-1}, E_\ell - \delta) \langle \ell | \rho_{\text{in}} | \ell \rangle, \quad (\text{E3})$$

$$P(+_0, \dots, +_{M-1}, x) = \left\{ \frac{\sin(2^M t_0 x)}{2^M \sin(t_0 x)} \right\}^2. \quad (\text{E4})$$

The success probability of the protocol is $p_{\text{mc}} \equiv \sum_\ell p_\ell$. The expressions (E3) and (E4) are used in Sec. III B 1.

Appendix F: Shot noise in SFF Measurements

Here we determine the shot noise in the SFF measurement. As described in Secs. III and IV, the measurement of the SFF involves the estimation of the expectation values $\langle \sigma^{x,y} \rangle$ for the control qubit by averaging results of N measurements. The statistical properties of such averaging can be described by introducing N copies of the control qubit and the spin system and considering the fluctuations of the collective spin $S_{x,y} = N^{-1} \sum_{k=1}^N \sigma_k^{x,y}$ of the N control qubits. In particular, we consider each copy of the control qubit and spin system to be initialized in the states $|+\rangle = \frac{1}{\sqrt{2}}(|0\rangle + |1\rangle)$ and ρ_{in} , respectively, and entangled via a controlled unitary $\mathcal{U}(\tau) = U(\tau) \otimes |0\rangle\langle 0| + \mathbb{I} \otimes |1\rangle\langle 1|$. In the case Hamiltonian dynamics we have $\mathcal{U}(\tau) = e^{-i\mathcal{H}_{\text{QND}}\tau}$ and, consequently, $U(\tau) = e^{-iH_{\text{spin}}\tau}$. Since we are interested in the noise due to a finite number of measurements, in what follows we consider a specific and fixed realization of disorder in the Hamiltonian H_{spin} .

After the QND interaction, the state of the N copies of the systems reads

$$\rho(\tau) = [\mathcal{U}(\tau) \rho_{\text{in}} \otimes |+\rangle\langle +| \mathcal{U}(\tau)^\dagger]^{\otimes N}.$$

The consecutive measurements of the control qubits yield an averaged outcome which is given by an eigenvalue $m_{x,y}$ of the observable $S_{x,y}$. The statistical distribution of

the outcomes $m_{x,y}$ is characterized by the corresponding moments of the collective spin observables with respect to the state $\rho(\tau)$.

The mean values read

$$\langle S_x(\tau) \rangle = \frac{1}{N} \sum_{k=1}^N \text{Tr} \{ \rho(\tau) (\mathbb{I} \otimes |0\rangle_k \langle 1| + \mathbb{I} \otimes |1\rangle_k \langle 0|) \}$$

$$= \frac{1}{2} \text{Tr} \{ \rho_{\text{in}} [U(\tau) + U(\tau)^\dagger] \} = \text{Re} \langle U(\tau) \rangle,$$

$$\langle S_y(\tau) \rangle = \text{Im} \langle U(\tau) \rangle,$$

where we expressed the operators $\sigma_k^{x,y}$ explicitly in the basis $|0(1)\rangle_k$ of k th control qubit. Thus, one can use the first moments to evaluate the average of the unitary operator $\langle U(\tau) \rangle = \langle S_x(\tau) \rangle + i \langle S_y(\tau) \rangle \approx m_x + im_y$.

The second and fourth moments of S_x read

$$\langle S_x^2(\tau) \rangle = \frac{1}{N^2} \left\{ N(N-1) [\text{Re} \langle U(\tau) \rangle]^2 + N \right\},$$

$$\langle S_x^4(\tau) \rangle = \frac{1}{N^4} \left\{ N(N-1)(N-2)(N-3) [\text{Re} \langle U(\tau) \rangle]^4 \right.$$

$$\left. + 2N(N-1)(3N-4) [\text{Re} \langle U(\tau) \rangle]^2 + N(3N-2) \right\}.$$

This result and similar expressions for S_y allows us to express the SFF and its fluctuations (for a single disorder realization) as

$$K(\tau) \equiv [\text{Re} \langle U(\tau) \rangle]^2 + [\text{Im} \langle U(\tau) \rangle]^2$$

$$= \frac{N}{N-1} \left(\langle S_x^2(\tau) \rangle + \langle S_y^2(\tau) \rangle - \frac{2}{N} \right)$$

$$\approx m_x^2 + m_y^2 - \frac{2}{N} \pm \mathcal{O} \left(\frac{1}{N} \right).$$

More precisely, the variance of the SFF estimation for $N \gg 1$ reads

$$\text{var} [K(\tau)] = \left\langle [S_x(\tau)^2 + S_y(\tau)^2]^2 \right\rangle - [\langle S_x^2(\tau) \rangle + \langle S_y^2(\tau) \rangle]^2$$

$$\approx \frac{4}{N} K(\tau) + \frac{4}{N^2}.$$

The signal-to-noise-ratio is thus given by $\text{SNR} \equiv K(\tau)/\sqrt{\text{var} [K(\tau)]}$. The SNR grows linearly $\text{SNR} \sim K(\tau)N/2$ with N up to $N \sim 2(1 + \sqrt{2})/K(\tau)$ where the SNR becomes 1. For a given number N of measurements and a fixed disorder, values of the SFF above the threshold of $K_*^{(1)} \equiv 2(1 + \sqrt{2})/N$ can thus be determined with an SNR that is larger than 1. The threshold value averaged over N_d realization of disorder $K_* = K_*^{(1)}/\sqrt{N_d}$ is presented in Sec. III B 3 and shown as horizontal lines in Figs. 3 and 6. A further increase of the number of measurements results in a slower growth with $\text{SNR} \sim \sqrt{K(\tau)N}/2$.

Appendix G: Recycling of the microcanonical state in the SFF measurement

In the Appendix we show that the SFF can be measured sequentially at different times τ_i using a single initial state

ρ_{mc} . Since the state ρ_{mc} is diagonal in the energy basis it commutes with the QND Hamiltonian (1). Therefore, the state is not perturbed after averaging over measurement results for a certain time τ :

$$\begin{aligned}\rho_{\text{out}} &= \mathcal{M}(+, \tau, \delta)\rho_{\text{mc}}\mathcal{M}^\dagger(+, \tau, \delta) \\ &+ \mathcal{M}(-, \tau, \delta)\rho_{\text{mc}}\mathcal{M}^\dagger(-, \tau, \delta) \\ &= \rho_{\text{mc}}.\end{aligned}$$

Here $\mathcal{M}(\pm, \tau, \delta)$ are the measurement operators defined in Eqs. (E1) and (E2).

Consequently, one can recycle the prepared microcanonical state as long as the decoherence in the spin system is negligible $\sum_i \tau_i \ll t_{\text{coh}}$. Furthermore, the above applies to any initial state as only the diagonal part of its density matrix contribute to the SFF. This result is used in the Sec. III B 2 and III B 4.

Appendix H: Measurement of the Heisenberg time

In this Appendix, we show how the Heisenberg time τ_{H} and the late-time plateau of the SFF K_∞ can be obtained from the probability p_{mc} with which the preparation of a microcanonical ensemble as described in Sec. III B 1 succeeds. Since the RMT form of the SFF is fully determined by these two parameters, the method we describe in the following can be used to validate the unbiased measurement of the SFF according to Sec. III in the regime in which RMT is applicable.

The preparation scheme assumes that the spin system is initialized in the infinite temperature state $\rho_\infty = \mathcal{D}^{-1} \sum_{\ell=1}^{\mathcal{D}} |\ell\rangle \langle \ell|$, where \mathcal{D} is the Hilbert space dimension and $|\ell\rangle$ are the eigenstates of the spin Hamiltonian. A microcanonical ensemble can then be prepared through M successive projections of the control qubit to the state $|+\rangle$, which occur each time after it the control qubit has been

entangled with the spin system. The success probability for this procedure reads

$$\begin{aligned}p_{\text{mc}} &= \frac{1}{\mathcal{D}} \sum_{\ell} P_{+M}(E_\ell - \delta) \\ &\approx \frac{1}{\mathcal{D}} \frac{1}{t_0 \delta_E} \int_{-1}^1 P_{+M}(x) dx \equiv \frac{1}{\mathcal{D}} \frac{1}{t_0 \delta_E} \mathcal{I}_M,\end{aligned}\quad (\text{H1})$$

where the filter function $P_{+M}(x)$ is given by the Eq. (14) and δ_E is the mean level spacing. Here we assume that the filter function is narrow enough such that smooth changes in the density of states can be neglected. For $M \gg 1$, the integral \mathcal{I}_M converges to $\pi 2^{-M}$. Therefore, the mean level spacing can be found as

$$\delta_E \approx \frac{\mathcal{I}_M}{\mathcal{D} p_{\text{mc}}} \frac{1}{t_0} \approx \frac{\pi 2^{-M}}{\mathcal{D} p_{\text{mc}}} \frac{1}{t_0},$$

and the corresponding Heisenberg time reads

$$\tau_{\text{H}} \equiv \frac{2\pi}{\delta_E} \approx 2^{M+1} t_0 \mathcal{D} p_{\text{mc}}.\quad (\text{H2})$$

The late-time plateau of the SFF can be estimated in a similar way. It is given by

$$\begin{aligned}K_\infty &= \sum_{\ell} f(E_\ell)^2 = \frac{1}{Z^2} \sum_{\ell} P_{+M}(E_\ell - \delta)^2 \\ &\approx \frac{1}{Z^2} \frac{1}{t_0 \delta_E} \int_{-1}^1 P_{+M}(x)^2 dx \equiv \frac{\mathcal{S}_M}{Z^2} \frac{1}{t_0 \delta_E}\end{aligned}$$

where $Z \equiv \sum_{\ell} P_{+M}(E_\ell - \delta) \approx \mathcal{I}_M / (t_0 \delta_E)$. Taking into account that the integral \mathcal{S}_M converges to $\pi 2^{1-M} / 3$ for $M \gg 1$ and using the expression for p_{mc} [Eq. (H1)] we obtain

$$K_\infty \approx \frac{\mathcal{S}_M}{\mathcal{I}_M^2} t_0 \delta_E \approx \frac{\mathcal{S}_M}{\mathcal{I}_M} \frac{1}{\mathcal{D} p_{\text{mc}}} \approx \frac{2}{3} \frac{1}{\mathcal{D} p_{\text{mc}}}.\quad (\text{H3})$$

Equations (H2) and (H3) are used in the Sec. III B 1 to uniquely fix the RMT prediction using experimental data.

-
- [1] Henning Labuhn, Daniel Barredo, Sylvain Ravets, Sylvain de Léséleuc, Tommaso Macrì, Thierry Lahaye, and Antoine Browaeys, “Tunable two-dimensional arrays of single rydberg atoms for realizing quantum ising models,” *Nature* **534**, 667–670 (2016).
- [2] M. A. Norcia, A. W. Young, and A. M. Kaufman, “Microscopic control and detection of ultracold strontium in optical-tweezer arrays,” *Phys. Rev. X* **8**, 041054 (2018).
- [3] Alexandre Cooper, Jacob P. Covey, Ivaylo S. Madjarov, Sergey G. Porsev, Marianna S. Safronova, and Manuel Endres, “Alkaline-earth atoms in optical tweezers,” *Phys. Rev. X* **8**, 041055 (2018).
- [4] Daniel Barredo, Vincent Lienhard, Sylvain de Léséleuc, Thierry Lahaye, and Antoine Browaeys, “Synthetic three-dimensional atomic structures assembled atom by atom,”

Nature **561**, 79–82 (2018).

- [5] Elmer Guardado-Sanchez, Peter T. Brown, Debayan Mitra, Trithip Devakul, David A. Huse, Peter Schauf, and Waseem S. Bakr, “Probing the quench dynamics of antiferromagnetic correlations in a 2d quantum ising spin system,” *Phys. Rev. X* **8**, 021069 (2018).
- [6] A. Omran, H. Levine, A. Keesling, G. Semeghini, T. T. Wang, S. Ebadi, H. Bernien, A. S. Zibrov, H. Pichler, S. Choi, J. Cui, M. Rossignolo, P. Rembold, S. Montangero, T. Calarco, M. Endres, M. Greiner, V. Vuletić, and M. D. Lukin, “Generation and manipulation of Schrödinger cat states in Rydberg atom arrays,” *Science* **365**, 570–574 (2019).
- [7] Sylvain de Léséleuc, Vincent Lienhard, Pascal Scholl, Daniel Barredo, Sebastian Weber, Nicolai Lang, Hans Pe-

- ter Büchler, Thierry Lahaye, and Antoine Browaeys, “Observation of a symmetry-protected topological phase of interacting bosons with Rydberg atoms,” *Science* **365**, 775–780 (2019).
- [8] Antoine Browaeys and Thierry Lahaye, “Many-body physics with individually controlled Rydberg atoms,” *Nat. Phys.* **16**, 132–142 (2020).
- [9] Martin Gärttner, Justin G. Bohnet, Arghavan Safavi-Naini, Michael L. Wall, John J. Bollinger, and Ana Maria Rey, “Measuring out-of-time-order correlations and multiple quantum spectra in a trapped-ion quantum magnet,” *Nat. Phys.* **13**, 781–786 (2017).
- [10] K. A. Landsman, C. Figgatt, T. Schuster, N. M. Linke, B. Yoshida, N. Y. Yao, and C. Monroe, “Verified quantum information scrambling,” *Nature* **567**, 61–65 (2019).
- [11] Andreas Elben, Benoît Vermersch, Rick van Bijnen, Christian Kokail, Tiff Brydges, Christine Maier, Manoj K. Joshi, Rainer Blatt, Christian F. Roos, and Peter Zoller, “Cross-platform verification of intermediate scale quantum devices,” *Phys. Rev. Lett.* **124**, 010504 (2020).
- [12] R. Barends, A. Shabani, L. Lamata, J. Kelly, A. Mezza-capo, U. Las Heras, R. Babbush, A. G. Fowler, B. Campbell, Yu Chen, Z. Chen, B. Chiaro, A. Dunsworth, E. Jeffrey, E. Lucero, A. Megrant, J. Y. Mutus, M. Neeley, C. Neill, P. J. J. O’Malley, C. Quintana, P. Roushan, D. Sank, A. Vainsencher, J. Wenner, T. C. White, E. Solano, H. Neven, and John M. Martinis, “Digitized adiabatic quantum computing with a superconducting circuit,” *Nature* **534**, 222–226 (2016).
- [13] Chao Song, Kai Xu, Hekang Li, Yu-Ran Zhang, Xu Zhang, Wuxin Liu, Qiujiang Guo, Zhen Wang, Wenhui Ren, Jie Hao, Hui Feng, Heng Fan, Dongning Zheng, Da-Wei Wang, H. Wang, and Shi-Yao Zhu, “Generation of multicomponent atomic schrödinger cat states of up to 20 qubits,” *Science* **365**, 574–577 (2019).
- [14] Maxwell F. Parsons, Anton Mazurenko, Christie S. Chiu, Geoffrey Ji, Daniel Greif, and Markus Greiner, “Site-resolved measurement of the spin-correlation function in the fermi-hubbard model,” *Science* **353**, 1253–1256 (2016).
- [15] Martin Boll, Timon A. Hilker, Guillaume Salomon, Ahmed Omran, Jacopo Nespolo, Lode Pollet, Immanuel Bloch, and Christian Gross, “Spin- and density-resolved microscopy of antiferromagnetic correlations in fermi-hubbard chains,” *Science* **353**, 1257–1260 (2016).
- [16] Christian Gross and Immanuel Bloch, “Quantum simulations with ultracold atoms in optical lattices,” *Science* **357**, 995–1001 (2017).
- [17] Matthew A. Norcia, Aaron W. Young, William J. Eckner, Eric Oelker, Jun Ye, and Adam M. Kaufman, “Seconds-scale coherence on an optical clock transition in a tweezer array,” *Science* **366**, 93–97 (2019), arXiv:1904.10934.
- [18] Raphael Kaubruegger, Pietro Silvi, Christian Kokail, Rick van Bijnen, Ana Maria Rey, Jun Ye, Adam M. Kaufman, and Peter Zoller, “Variational spin-squeezing algorithms on programmable quantum sensors,” *Phys. Rev. Lett.* **123**, 260505 (2019).
- [19] An alternative definition is $\mathcal{H}_{\text{QND}} = H_{\text{spin}} \otimes \sigma_c^z$ with Pauli operator σ_c^z . However, we prefer the form (1) in light of the physical realization in Sec. II.
- [20] Michael A. Nielsen and Isaac L. Chuang, *Quantum Computation and Quantum Information: 10th Anniversary Edition*, 10th ed. (Cambridge University Press, USA, 2011).
- [21] G. Giedke, J. M. Taylor, D. D’Alessandro, M. D. Lukin, and A. Imamoglu, “Quantum measurement of a mesoscopic spin ensemble,” *Phys. Rev. A* **74**, 032316 (2006).
- [22] Krysta M. Svore, Matthew B. Hastings, and Michael Freedman, “Faster phase estimation,” *Quantum Inf. Comput.* **14**, 306–328 (2014).
- [23] G. Pupillo, A. Micheli, M. Boninsegni, I. Lesanovsky, and P. Zoller, “Strongly correlated gases of rydberg-dressed atoms: Quantum and classical dynamics,” *Phys. Rev. Lett.* **104**, 223002 (2010).
- [24] T. Macrì and T. Pohl, “Rydberg dressing of atoms in optical lattices,” *Phys. Rev. A* **89**, 011402 (2014).
- [25] A. W. Glaetzle, R. M. W. van Bijnen, P. Zoller, and W. Lechner, “A coherent quantum annealer with rydberg atoms,” *Nat. Commun.* **8**, 15813 (2017).
- [26] Y. Y. Jau, A. M. Hankin, T. Keating, I. H. Deutsch, and G. W. Biedermann, “Entangling atomic spins with a rydberg-dressed spin-flip blockade,” *Nat. Phys.* **12**, 71–74 (2016).
- [27] Johannes Zeiher, Rick van Bijnen, Peter Schauß, Sebastian Hild, Jae-yoon Choi, Thomas Pohl, Immanuel Bloch, and Christian Gross, “Many-body interferometry of a rydberg-dressed spin lattice,” *Nat. Phys.* **12**, 1095–1099 (2016).
- [28] V. Borish, O. Marković, J. A. Hines, S. V. Rajagopal, and M. Schleier-Smith, “Transverse-field ising dynamics in a rydberg-dressed atomic gas,” *Phys. Rev. Lett.* **124**, 063601 (2020).
- [29] Jordan S. Cotler, Guy Gur-Ari, Masanori Hanada, Joseph Polchinski, Phil Saad, Stephen H. Shenker, Douglas Stanford, Alexandre Streicher, and Masaki Tezuka, “Black holes and random matrices,” *J. High Energ. Phys.* **2017**, 118 (2017), arXiv:1611.04650.
- [30] Pavel Kos, Marko Ljubotina, and Tomaž Prosen, “Many-Body Quantum Chaos: Analytic Connection to Random Matrix Theory,” *Phys. Rev. X* **8**, 021062 (2018), arXiv:1712.02665.
- [31] J. Šuntajs, J. Bonča, T. Prosen, and L. Vidmar, “Quantum chaos challenges many-body localization,” (2019), arXiv:1905.06345.
- [32] D. A. Abanin, J. H. Bardarson, G. De Tomasi, S. Gopalakrishnan, V. Khemani, S. A. Parameswaran, F. Pollmann, A. C. Potter, M. Serbyn, and R. Vasseur, “Distinguishing localization from chaos: challenges in finite-size systems,” (2019), arXiv:1911.04501.
- [33] C. Senko, J. Smith, P. Richerme, A. Lee, W. C. Campbell, and C. Monroe, “Coherent imaging spectroscopy of a quantum many-body spin system,” *Science* **345**, 430–433 (2014).
- [34] P. Jurcevic, P. Hauke, C. Maier, C. Hempel, B. P. Lanyon, R. Blatt, and C. F. Roos, “Spectroscopy of Interacting Quasiparticles in Trapped Ions,” *Phys. Rev. Lett.* **115**, 100501 (2015).
- [35] P. Roushan, C. Neill, J. Tangpanitanon, V. M. Bastidas, A. Megrant, R. Barends, Y. Chen, Z. Chen, B. Chiaro, A. Dunsworth, A. Fowler, B. Foxen, M. Giustina, E. Jeffrey, J. Kelly, E. Lucero, J. Mutus, M. Neeley, C. Quintana, D. Sank, A. Vainsencher, J. Wenner, T. White, H. Neven, D. G. Angelakis, and J. Martinis, “Spectroscopic signatures of localization with interacting photons in superconducting qubits,” *Science* **358**, 1175–1179 (2017).
- [36] Alexander W. Glaetzle, Marcello Dalmonte, Rejish Nath, Christian Gross, Immanuel Bloch, and Peter Zoller, “De-

- signing frustrated quantum magnets with laser-dressed rydberg atoms,” *Phys. Rev. Lett.* **114**, 173002 (2015).
- [37] R. M. W. van Bijnen and T. Pohl, “Quantum magnetism and topological ordering via rydberg dressing near förster resonances,” *Phys. Rev. Lett.* **114**, 243002 (2015).
- [38] M. Müller, I. Lesanovsky, H. Weimer, H. P. Büchler, and P. Zoller, “Mesoscopic rydberg gate based on electromagnetically induced transparency,” *Phys. Rev. Lett.* **102**, 170502 (2009).
- [39] Hannes Pichler, Guanyu Zhu, Alireza Seif, Peter Zoller, and Mohammad Hafezi, “Measurement protocol for the entanglement spectrum of cold atoms,” *Phys. Rev. X* **6**, 041033 (2016).
- [40] Guanyu Zhu, Mohammad Hafezi, and Tarun Grover, “Measurement of many-body chaos using a quantum clock,” *Phys. Rev. A* **94**, 062329 (2016), arXiv:1607.00079.
- [41] F. Grusdt, N. Y. Yao, D. Abanin, M. Fleischhauer, and E. Demler, “Interferometric measurements of many-body topological invariants using mobile impurities,” *Nat. Commun.* **7**, 11994 (2016).
- [42] Maksym Serbyn and Dmitry A. Abanin, “Loschmidt echo in many-body localized phases,” *Phys. Rev. B* **96**, 014202 (2017).
- [43] Ron Belyansky, Jeremy T. Young, Przemyslaw Bienias, Zachary Eldredge, Adam M. Kaufman, Peter Zoller, and Alexey V. Gorshkov, “Nondestructive cooling of an atomic quantum register via state-insensitive rydberg interactions,” *Phys. Rev. Lett.* **123**, 213603 (2019).
- [44] Sylvain Ravets, Henning Labuhn, Daniel Barredo, Lucas Béguin, Thierry Lahaye, and Antoine Browaeys, “Coherent dipole–dipole coupling between two single Rydberg atoms at an electrically-tuned Förster resonance,” *Nat. Phys.* **10**, 914–917 (2014).
- [45] Fritz Haake, *Quantum Signatures of Chaos*, Springer Series in Synergetics, Vol. 54 (Springer Berlin Heidelberg, Berlin, Heidelberg, 2010).
- [46] Arijeet Pal and David A. Huse, “Many-body localization phase transition,” *Phys. Rev. B* **82**, 174411 (2010).
- [47] David J. Luitz, Nicolas Laflorencie, and Fabien Alet, “Many-body localization edge in the random-field Heisenberg chain,” *Phys. Rev. B* **91**, 081103 (2015).
- [48] Luca D’Alessio, Yariv Kafri, Anatoli Polkovnikov, and Marcos Rigol, “From quantum chaos and eigenstate thermalization to statistical mechanics and thermodynamics,” *Adv. Phys.* **65**, 239–362 (2016), arXiv:1509.06411.
- [49] Madan Lal Mehta, *Random Matrices*, 3rd ed. (Academic Press, 2004) p. 706.
- [50] Liangsheng Zhang, Vedika Khemani, and David A. Huse, “A Floquet model for the many-body localization transition,” *Phys. Rev. B* **94**, 224202 (2016).
- [51] Bruno Bertini, Pavel Kos, and Tomaž Prosen, “Exact Spectral Form Factor in a Minimal Model of Many-Body Quantum Chaos,” *Phys. Rev. Lett.* **121**, 264101 (2018), arXiv:1805.00931.
- [52] Amos Chan, Andrea De Luca, and J. T. Chalker, “Solution of a Minimal Model for Many-Body Quantum Chaos,” *Phys. Rev. X* **8**, 41019 (2018).
- [53] Amos Chan, Andrea De Luca, and J. T. Chalker, “Spectral Statistics in Spatially Extended Chaotic Quantum Many-Body Systems,” *Phys. Rev. Lett.* **121**, 60601 (2018).
- [54] Nicolas Regnault and Rahul Nandkishore, “Floquet thermalization: Symmetries and random matrix ensembles,” *Phys. Rev. B* **93**, 104203 (2016), arXiv:1510.07653.
- [55] Toshiya Kinoshita, Trevor Wenger, and David S Weiss, “A quantum Newton’s cradle,” *Nature* **440**, 900–903 (2006).
- [56] M. Gring, M. Kuhnert, T. Langen, T. Kitagawa, B. Rauer, M. Schreitl, I. Mazets, D. A. Smith, E. Demler, and J. Schmiedmayer, “Relaxation and Prethermalization in an Isolated Quantum System,” *Science* **337**, 1318–1322 (2012).
- [57] Tim Langen, Sebastian Erne, Remi Geiger, Bernhard Rauer, Thomas Schweigler, Maximilian Kuhnert, Wolfgang Rohringer, Igor E. Mazets, Thomas Gasenzer, and Jörg Schmiedmayer, “Experimental observation of a generalized Gibbs ensemble,” *Science* **348**, 207–211 (2015), arXiv:1411.7185.
- [58] Michael Schreiber, Sean S Hodgman, Pranjal Bordia, H. P. Luschen, Mark H Fischer, Ronen Vosk, Ehud Altman, Ulrich Schneider, and Immanuel Bloch, “Observation of many-body localization of interacting fermions in a quasirandom optical lattice,” *Science* **349**, 842–845 (2015).
- [59] J.-y. Choi, S. Hild, J. Zeiher, P. Schauss, A. Rubio-Abadal, T. Yefsah, V. Khemani, D. A. Huse, I. Bloch, and C. Gross, “Exploring the many-body localization transition in two dimensions,” *Science* **352**, 1547–1552 (2016).
- [60] J. Smith, A. Lee, P. Richerme, B. Neyenhuis, P. W. Hess, P. Hauke, M. Heyl, D. A. Huse, and C. Monroe, “Many-body localization in a quantum simulator with programmable random disorder,” *Nat. Phys.* **12**, 907–911 (2016).
- [61] Kai Xu, Jin-Jun Chen, Yu Zeng, Yu-Ran Zhang, Chao Song, Wuxin Liu, Qiujiang Guo, Pengfei Zhang, Da Xu, Hui Deng, Keqiang Huang, H. Wang, Xiaobo Zhu, Dongning Zheng, and Heng Fan, “Emulating Many-Body Localization with a Superconducting Quantum Processor,” *Phys. Rev. Lett.* **120**, 050507 (2018).
- [62] Alexander Lukin, Matthew Rispoli, Robert Schittko, M. Eric Tai, Adam M. Kaufman, Soonwon Choi, Vedika Khemani, Julian Léonard, and Markus Greiner, “Probing entanglement in a many-body-localized system,” *Science* **364**, 256–260 (2019).
- [63] Tiff Brydges, Andreas Elben, Petar Jurcevic, Benoît Vermersch, Christine Maier, Ben P. Lanyon, Peter Zoller, Rainer Blatt, and Christian F. Roos, “Probing Rényi entanglement entropy via randomized measurements,” *Science* **364**, 260–263 (2019).
- [64] Andrew J. Daley, Martin M. Boyd, Jun Ye, and Peter Zoller, “Quantum computing with alkaline-earth-metal atoms,” *Phys. Rev. Lett.* **101**, 170504 (2008).
- [65] R Mukherjee, J Millen, R Nath, M P A Jones, and T Pohl, “Many-body physics with alkaline-earth rydberg lattices,” *J. Phys. B: At. Mol. Opt.* **44**, 184010 (2011).
- [66] Ivaylo S. Madjarov, Jacob P. Covey, Adam L. Shaw, Joonhee Choi, Anant Kale, Alexandre Cooper, Hannes Pichler, Vladimir Schkolnik, Jason R. Williams, and Manuel Endres, “High-fidelity entanglement and detection of alkaline-earth rydberg atoms,” *Nat. Phys.* (2020), 10.1038/s41567-020-0903-z.
- [67] Dayou Yang, Andrey Grankin, Lukas M. Sieberer, Denis V. Vasilyev, and Peter Zoller, “Quantum non-demolition measurement of a many-body Hamiltonian,” *Nat. Commun.* **11**, 775 (2020), arXiv:1905.06444.
- [68] Dries Sels and Eugene Demler, “Quantum generative model for sampling many-body spectral functions,” *Phys. Rev. Lett.* **123**, 1–6 (2019), arXiv:1910.14213.
- [69] Dries Sels, Hesam Dashti, Samia Mora, Olga Demler, and Eugene Demler, “Quantum approximate

- Bayesian computation for NMR model inference,” (2019), [arXiv:1910.14221](https://arxiv.org/abs/1910.14221).
- [70] Nikola Šibalić, Jonathan D Pritchard, Charles S Adams, and Kevin J Weatherill, “Arc: An open-source library for calculating properties of alkali rydberg atoms,” *Comput. Phys. Commun.* **220**, 319–331 (2017).
- [71] M. Saffman, T. G. Walker, and K. Mølmer, “Quantum information with rydberg atoms,” *Rev. Mod. Phys.* **82**, 2313–2363 (2010).
- [72] B. Vermersch, A. W. Glaetzle, and P. Zoller, “Magic distances in the blockade mechanism of rydberg p and d states,” *Phys. Rev. A* **91**, 023411 (2015).
- [73] Rick van Bijnen, *Quantum engineering with ultracold atoms*, *Ph.D. thesis*, Technische Universiteit Eindhoven (2013).
- [74] Florentin Reiter and Anders S. Sørensen, “Effective operator formalism for open quantum systems,” *Phys. Rev. A* **85**, 032111 (2012).
- [75] Jordan Cotler, Nicholas Hunter-Jones, Junyu Liu, and Beni Yoshida, “Chaos, complexity, and random matrices,” *J. High Energ. Phys.* **2017**, 48 (2017), [arXiv:1706.05400](https://arxiv.org/abs/1706.05400).